NACA

RESEARCH MEMORANDUM

COMPARISON OF PERFORMANCE OF TWO AERODYNAMICALLY SIMILAR 14-INCH-DIAMETER SINGLE-STAGE COMPRESSOR ROTORS OF DIFFERENT CHORD LENGTH

By Marvin I. Kussoy and Daniel Bachkin

Lewis Flight Propulsion Laboratory
Cleveland, Ohio

NATIONAL ADVISORY COMMITTEE
FOR AERONAUTICS

WASHINGTON
February 10, 1958

[redacted]

NATIONAL ADVISORY COMMITTEE FOR AERONAUTICS

RESEARCH MEMORANDUM

COMPARISON OF PERFORMANCE OF TWO AERODYNAMICALLY SIMILAR 14-INCH-DIAMETER SINGLE-STAGE COMPRESSOR ROTORS OF DIFFERENT CHORD LENGTH

By Marvin I. Kussoy and Daniel Bachkin

SUMMARY

The performance of two aerodynamically similar single-stage rotors of different chord length was compared. The short-chord rotor was of a design typical for a last stage of a multistage compressor. The long-chord rotor, with a chord 2.5 times that of the short-chord rotor, achieved a higher pressure ratio and operated over a greater equivalent-weight-flow range than the short-chord rotor at every speed investigated. The equivalent weight flow of the long-chord rotor was lower at the peak-pressure-ratio end and higher at the low-pressure-ratio end of the performance curves. The two rotors had approximately the same peak efficiencies. The stall and surge characteristics were similar, both rotors experiencing abrupt stall as the flow was decreased. The pressure ratio after stall decreased to the same value for both rotors.

In the range of Reynolds numbers investigated, there was some effect on performance as Reynolds number was decreased, but this effect accounted for only a small part of the difference in the performance of the two rotors at the same inlet pressure. An analysis of various diffusion parameters indicated that the better performance of the long-chord rotor could be due to either a chord or an aspect-ratio effect.

INTRODUCTION

The rear stages of a multistage axial-flow compressor must operate over a wide range of conditions. For a fixed-geometry compressor at part-speed operation, choking can occur in the rear stages that may eventually lead to stall in the inlet stages. During overspeed operation, stall may occur in the rear stages. Thus it appears that a rear stage designed to have a wider range of stall-free and choke-free operation would alleviate undesirable influences on the off-design performance of a

[redacted]

multistage compressor. Consequently, a part of the compressor research program at the NACA Lewis laboratory is directed toward a search for compressor designs having these favorable characteristics. The object of the study reported herein was to determine the effect of chord length on the performance of a rotor designed to be representative of a rear stage of a multistage compressor.

The facilities available placed some limits on permissible blade chord lengths. Considering these limits, the representative rotor was designed for a blade chord length of 0.67 inch, and the second rotor was designed with a chord of 1.67 inches (2.5 times that of the representative rotor). These chord lengths correspond to aspect ratios of 2.09 and 0.84. The solidity of both rotors is the same.

Both rotors were tested at five speeds from 53 to 100 percent of design equivalent speed, with an absolute inlet pressure of 25 inches of mercury. Some additional data were taken at lower inlet pressures for the long-chord rotor at the two highest speeds and for the short-chord rotor at design speed. At each speed, performance data were obtained for a range of weight flows from the minimum obtainable with the throttling system to the flow required for a pressure ratio near 1.0. This report presents and compares the over-all performance, stall characteristics, and blade-element parameters of the two rotors.

ROTOR DESIGN

A rotor was designed that would be representative of a typical rotor in the rear stages of a multistage axial-flow compressor. The design values are as follows:

Hub-tip radius ratio	0.8
Aspect ratio	2.1
Tip diffusion factor	0.4
Tip solidity	≈1.0
Equivalent tip speed, ft/sec	850
Relative inlet-air angle at tip, deg	65
Adiabatic temperature-rise efficiency	0.88

A 14-inch tip diameter was specified in order to utilize existing facilities.

A straight passage with no hub or tip curvature was specified to eliminate any radial-flow effects due to curvature. Since no whirl was used at the inlet to the rotor, the axial velocity was considered constant from hub to tip. Neglecting the effects of entropy gradients, the axial velocity at the rotor outlet was constant with respect to radius, because radially constant energy addition was used through the rotor.

[redacted]

These specifications and assumptions provided sufficient information to perform all calculations required by the method described in reference 1 (ch. IX) to determine the discharge velocity diagram. The computed discharge axial velocity resulted in an axial velocity ratio across the rotor of slightly less than 1.0. It was then possible to compute the discharge relative air angle at any radial position. The method given in reference 1 (ch. VII) was used to obtain design incidence and deviation angles. Double-circular-arc blades with constant chord from hub to tip were used.

All blade coordinates were scaled up 2.5 times to obtain a second rotor with a blade chord length 2.5 times that of the representative rotor. Only the values of chord, aspect ratio, and spacing were different for the long-chord rotor. The two rotor assemblies are shown in figure 1. Long- and short-chord blades are shown in figure 2. The pertinent design details for both rotors are listed in table I.

APPARATUS AND INSTRUMENTATION

Test Facility

The test facility used in this investigation (fig. 3) is similar to that described in reference 2.

Over-All Performance Instrumentation

Radial survey data were taken at instrumentation stations 1 and 2 (fig. 3). Station 1 was approximately 1/2 inch upstream of the rotor leading edge, and station 2 was approximately 1/2 chord length downstream of the rotor trailing edge. A combination probe for measuring total pressure, total temperature, and flow angle, and a probe for measuring static pressure were used at stations 1 and 2. The probes were installed in actuators that were automatically self-alining so that the probes were always oriented in the flow direction. Static pressure was also measured at the casing inner and outer walls before and after the rotor.

Rotating-Stall and Surge Instrumentation

Constant-temperature hot-wire anemometers were used for detecting rotating stall and surge. Hot-wire probes with 0.0002-inch-diameter tungsten wires mounted parallel to the axis of the probe and an effective length of 0.080 inch were used. The probes could be traversed so that the radial extent of the stall zones could be ascertained. Detailed descriptions of the equipment and techniques involved are presented in references 3 and 4. An audiofrequency oscillator was used in conjunction with an oscilloscope to determine the frequency of rotating stall or surge.

PROCEDURE

Each rotor was tested at equivalent tip speeds of 850, 750, 650, 550, and 450 feet per second (100, 88.2, 76.5, 64.7, and 52.9 percent of design equivalent speed, respectively). At each speed, performance data were obtained for a flow range between the minimum obtainable with the throttling system to a flow required for a pressure ratio near 1.0. These performance data were for an absolute inlet pressure of 25 inches of mercury. The long-chord rotor was also operated at the two highest speeds at lower inlet pressures to give a Reynolds number range comparable to that encountered with the short-chord rotor. In addition, some data were obtained over a range of inlet pressures at design speed to ascertain the effect of Reynolds number on the performance of both rotors.

Total and static pressure, total temperature, and flow angle were measured at stations 1 and 2 at the tip, mean, and hub (0.2, 0.7, and 1.2 in. from the outer casing; 85.7, 50.0, and 14.3 percent of the passage height from the inner wall, respectively).

During stall operation, hot-wire anemometers were used to examine surge and stall flow characteristics over the entire passage. Inaudible high-frequency surge was distinguished from rotating stall by the inability to detect any phase shift by the method described in reference 5. The instruments indicated the changes in flow characteristics that occurred when rotating stall or surge was encountered or when stall or surge frequencies changed. Observations were made as flow was increased and decreased. The hot-wire signals were photographed before and after the flow changes.

RESULTS AND DISCUSSION

The over-all performance data at an inlet pressure of 25 inches of mercury are presented first for each rotor, and these data are compared. The effect on rotor performance of operating at various inlet pressures is then discussed, and blade-element data for the two rotors are compared. Finally, separation criteria are analyzed for a possible explanation of the differences in rotor performance.

Short-Chord-Rotor Performance

Over-all performance. - The data obtained for the short-chord rotor at an inlet pressure of 25 inches of mercury are presented in figure 4(a) as a plot of mass-averaged adiabatic temperature-rise efficiency and mass-averaged total-pressure ratio against equivalent weight flow. A maximum mass-averaged pressure ratio of 1.21 was achieved at the design

tip speed. The equivalent weight flow and the mass-averaged adiabatic efficiency at this point were 9.75 pounds per second and 0.833, respectively.

The peak efficiency for design speed was 0.88 at a pressure ratio of about 1.15. At design speed, the weight-flow range from peak pressure ratio to a pressure ratio near 1.0 was 2.57 pounds per second.

A flow-range parameter can be defined as follows:

$$\text{Percent flow range} = \frac{\left(\frac{w_o\sqrt{\theta_o}}{\delta_o}\right)_{\frac{\overline{P}_2}{\overline{P}_1}\approx 1} - \left(\frac{w_o\sqrt{\theta_o}}{\delta_o}\right)_{\text{Incipient stall}}}{\left(\frac{w_o\sqrt{\theta_o}}{\delta_o}\right)_{\frac{\overline{P}_2}{\overline{P}_1}\approx 1}}$$

(Symbols are defined in appendix A.) Using this definition of range, the percent flow range increased from 20.9 percent at design speed to 37.2 percent at the lowest speed tested. For all speeds, the rotor efficiencies were greater than 84 percent for more than 55 percent of the weight-flow range from $\left(\frac{w_o\sqrt{\theta_o}}{\delta_o}\right)_{\frac{\overline{P}_2}{\overline{P}_1}\approx 1}$ to $\left(\frac{w_o\sqrt{\theta_o}}{\delta_o}\right)_{\text{Incipient stall}}$.

Stall. - An abrupt change in performance occurred at all speeds when rotating stall was encountered. The magnitude of the pressure drop and of the decrease in efficiency is evident in figure 4(a). An initial rotating stall of one zone extending from tip to hub occurred at all speeds. As the flow was reduced, the number of zones increased to a maximum of two zones for the two highest speeds and progressed to a maximum of four zones for the other speeds. Further decrease in flow resulted in surge for all but the lowest speed. Because of the inaccuracy of data obtained in surge operation, these points are not presented in figure 4(a). The number of stall zones was determined by the method described in reference 5. For the lowest speed, after rotating stall was encountered, it was necessary to increase the flow to a value above that of the incipient-stall point before rotating stall was eliminated; the hysteresis loop was thus produced. For all other speeds, stalling and unstalling occurred at about the same weight flow.

Long-Chord-Rotor Performance

Over-all performance. - The mass-averaged adiabatic temperature-rise efficiency and mass-averaged total-pressure ratio are plotted against equivalent weight flow for the long-chord rotor at an absolute inlet pressure of 25 inches of mercury in figure 4(b). At the maximum pressure ratio of 1.24 for the design speed, the equivalent weight flow and efficiency were 8.9 pounds per second and 0.833, respectively. The peak efficiency for the design speed was 0.887 at a pressure ratio of 1.20. At design speed, the flow range from peak pressure ratio to a pressure ratio near 1.0 was 4.10 pounds per second. The percent flow range increased from 31.5 percent at design speed to 44.4 percent at the lowest speed tested. For more than 55 percent of the weight-flow range from $\left(\frac{w_o\sqrt{\theta_o}}{\delta_o}\right)_{\substack{\text{Incipient}\\ \text{stall}}}$ to $\left(\frac{w_o\sqrt{\theta_o}}{\delta_o}\right)_{\frac{\overline{P}_2}{\overline{P}_1}\approx 1}$ the rotor efficiencies were greater than 85 percent for all speeds.

Stall. - An abrupt change in performance occurred when rotating stall or surge was detected by means of hot wires. A noticeable drop in pressure ratio and efficiency occurred for all speeds as rotating stall or surge was encountered (fig. 4(b)). A single-zone total-span rotating stall occurred initially for all but the highest speed. The number of rotating-stall zones first increased from one zone to two zones as the flow was decreased. Surge was eventually encountered at all speeds as the flow was further decreased. It was not possible to detect any rotating stall at the highest speed; only surge was encountered as the flow was decreased below the incipient-stall point. Only the three lowest speeds produced the characteristic of a hysteresis loop as the flow was increased when rotating stall was present.

Comparison of Over-All Performance

Inlet pressure of 25 inches of mercury. - Curves faired through the unstalled portion of the performance data in figures 4(a) and (b) are presented in figure 5 to facilitate comparison of the performances of the long- and short-chord rotors. At all speeds for both rotors, the point just before rotating stall or surge was encountered (the incipient-stall point) is also the point of peak pressure ratio. This is a typical characteristic described in reference 6 for a stage with high hub-tip radius ratio.

The curves in figure 5 show that the long-chord rotor has a higher pressure ratio for any given equivalent weight flow at all speeds. At design speed, and at the weight flow for which the short-chord rotor

produces its peak pressure ratio of 1.21 (9.75 lb/sec), the long-chord rotor attains a pressure ratio of 1.22 and still has not reached its peak of 1.24. The efficiency of the long-chord rotor at this point is 3.4 percentage points higher than that of the short-chord rotor (0.867 for the long-chord and 0.833 for the short-chord rotor).

The flow at a pressure ratio of 1.0 is higher for the long-chord than for the short-chord rotor, and the long-chord rotor can also operate at lower flows before rotating stall or surge is encountered. Except at the lowest speed, the long-chord rotor has a percent flow range between peak pressure ratio and a pressure ratio near 1.0 that is from 48 to 72 percent greater than that of the short-chord rotor. At the lowest speed the percent flow range of the long-chord rotor is about 20 percent greater than that of the short-chord rotor. For the speeds of 550 and 650 feet per second, about 60 percent of the increased weight-flow range is at the low-pressure-ratio end of the performance curves, while for the lowest speed 75 percent of the increased range is at the low-pressure-ratio end of the performance curves. The gain in range at the low-pressure-ratio end of the flow range is important, since rear-stage choking strongly influences the flow-handling capacity of a multistage compressor during part-speed operation. For the speeds of 750 and 850 feet per second, about 53 and 57 percent, respectively, of the increased weight-flow range is at the stall end of the flow range. Thus, undesirable influences of a rear stage operating in or very near stall during high-speed operation of a multistage compressor could be reduced by the use of the long-chord rotor.

Both rotors attain approximately the same peak efficiency (fig. 5). However, the long-chord rotor maintains higher values of efficiency over a greater weight-flow range.

An investigation of the effect of chord length on over-all compressor performance of a multistage compressor is reported in reference 7. Over-all compressor performance data are compared in reference 7 for two configurations that are identical except that the chord lengths in the first two stages of one are twice those in the other. Essentially, the difference in over-all performance maps for the two configurations indicates a change in performance of the first two stages. This indicated change (viz., a greater stall-free flow range for the long-chord inlet stages) is consistent with the results obtained from a comparison of the performance of the two rotors in the present report.

Effect of varying inlet pressure. - At the same inlet pressure, the two rotors operate at different Reynolds numbers because of their different chord lengths. Therefore, it might be concluded that the improvement in performance obtained with the long-chord rotor is due to increased Reynolds numbers. Consequently, a comparison of performance at comparable Reynolds numbers was desirable. For an inlet pressure of 10 inches

of mercury, the Reynolds number range for the long-chord rotor based on inlet relative velocity and chord length is 2.0×10^5 to 2.2×10^5 for the two highest speeds. This compares with the Reynolds number range of 2.0×10^5 to 2.3×10^5 for the short-chord rotor at the two highest speeds at an inlet pressure of 25 inches of mercury.

The unstalled portion of the performance data for the long-chord rotor at an inlet pressure of 10 inches of mercury is plotted in figure 6 for tip speeds of 750 and 850 feet per second. The mass-averaged adiabatic temperature-rise efficiencies and mass-averaged pressure ratios are plotted against integrated equivalent weight flow. Since the orifice was not changed during the entire investigation, the pressure drop across the orifice at the lower inlet pressure was in the range of values that might be questionable and could result in inaccurate values of equivalent weight flow. Therefore, integrated equivalent weight flows obtained at station 1 for the low-inlet-pressure long-chord data are plotted in figure 6. The data obtained at an inlet pressure of 25 inches of mercury for the two rotors are also plotted against integrated equivalent weight flow at station 1 in this figure to evaluate the effects of Reynolds number.

It is evident from figure 6 that there are some differences in the performance of the long-chord rotor at different Reynolds numbers. However, comparing the performance of the two rotors in the same Reynolds number range shows that the long-chord rotor still attains a higher pressure ratio and has a greater flow range between the peak- and low-pressure-ratio ends of the performance curve (in both lb/sec and % range). It is apparent that only part of the difference in performance for the long- and short-chord rotors can be attributed to a Reynolds number effect.

Some supplementary data were obtained in order to examine more fully the extent of Reynolds number effect on both rotors. Peak mass-averaged adiabatic temperature-rise efficiency points were determined for both rotors at various inlet pressures for the design tip speed. These peak-efficiency points are plotted against Reynolds number in figure 7. It is evident that there is only a slight Reynolds number effect on peak efficiency until the very low Reynolds numbers are encountered. A more detailed investigation and analysis of Reynolds number effect is made in reference 8, which covers a Reynolds number range of 8,000 to 50,000. Another investigation, using a single-stage free-vortex machine with an incompressible working fluid, covers a Reynolds number range of 2,000 to 150,000 (ref. 9). Although a direct comparison cannot be made between the data presented in figure 7 and the results presented in references 8 and 9, a qualitative comparison indicates that the long- and short-chord rotors operate in the range where Reynolds number has very little effect on single-stage compressors.

Blade-Element Performance

The conventional blade-element performance data are presented in figures 8 and 9 for the short- and long-chord rotor blades, respectively. The various parameters plotted in this figure are discussed in reference 1.

A faired curve of the total-pressure-loss coefficient $\bar{\omega}'$ against incidence angle i is presented in figure 10. This plot shows that at the mean and hub the level of $\bar{\omega}'$ for both rotor blades is about the same. At the tip, the minimum $\bar{\omega}'$ is about 0.04 for both blades. This value of $\bar{\omega}'_{min}$ occurs at an incidence angle of 2° for the short-chord blade and about -3.5° for the long-chord blade. For the short-chord rotor blade, $\bar{\omega}'$ increases on both sides of the minimum-loss incidence angle; whereas for the long-chord blade, it increases as incidence angle is increased. It should be noted that, at incidence angles higher than 2° at the tip, $\bar{\omega}'$ for the short-chord blades increases more rapidly until it encounters rotating stall. The maximum $\bar{\omega}'$ at the tip for the long-chord blade is higher than that for the short-chord blade, because rotating stall or surge is delayed with the long-chord blade, and thus the long-chord blade covers a wider incidence-angle range.

The incidence angles obtained at peak pressure ratio and at a pressure ratio near 1.0 at each speed and inlet pressure investigated are presented in figure 11. The faired curves of figure 11 represent the arithmetic average of the incidence angles at the hub, mean, and tip. At all speeds and at all radial positions, the incidence angle for the long-chord blade is lower at the low-pressure-ratio end and higher at the peak-pressure-ratio end of the performance curves than the incidence angle for the short-chord blade. At every speed and radial position the incidence-angle range of the long-chord blade at the inlet pressure of 25 inches of mercury is from about 4° to 6° wider than the range for the short-chord blade. The same trend is found for the incidence-angle range of the long-chord blade at the two higher speeds at an inlet pressure of 10 inches of mercury compared with the short-chord range at 25 inches of mercury. At this lower inlet pressure the incidence-angle range for the long-chord blade is also extended at both the peak-pressure-ratio and low-pressure-ratio ends of the curve and is about $2\frac{1}{2}^\circ$ to 4° wider than that of the short-chord blade. The magnitudes of the "average" incidence angles measured at the low inlet pressure are within $\frac{1}{2}^\circ$ to $1\frac{1}{2}^\circ$ of the values for the long-chord blade at the inlet pressure of 25 inches of mercury. Thus, lowering the Reynolds number of the long-chord blade to that of the short-chord blade does not account for all the difference in the incidence-angle range of the long- and short-chord blades at the same inlet pressure. This is in agreement with the over-all performance data.

[redacted]

Rotating Stall

The pertinent facts concerning the stall characteristics for the two rotors are listed in table II. Presented in the table are the surge frequencies, the number of rotating-stall zones detected, and the order in which they were encountered. The absolute propagation rate used in this table is the ratio of the absolute rotative speed of one zone divided by the rotative speed of one rotor blade. In this table, the observations are numbered in sequence for unique operating points. These numbered points do not necessarily correspond to the solid symbols presented in figure 4, which are shown only to indicate the trend in rotor performance as the flow rate is varied after rotating stall or surge is encountered. At each speed, a larger pressure drop occurs for the long-chord rotor than for the short-chord rotor as rotating stall or surge is encountered. Thus, for the same speed, both rotors are at about the same pressure ratio at flows lower than their respective incipient-stall points. It appears that the stall characteristics for both rotors are essentially the same.

Separation-Parameter Analysis

Various theories were investigated in order to explain the fact that the short-chord rotor consistently went into either rotating stall or surge at a higher weight flow than the long-chord rotor. Since it has been previously shown that the Reynolds number effect on these particular rotors accounts for only a part of the difference in stalling weight flow, it is hypothesized that any effect would be due to the change in aspect ratio or chord or a combination of both of these. Spacing was also changed; but, since $s = c/\sigma$, any spacing effect can be expressed as a constant times chord, since σ was held constant.

Two separation parameters, D_L and D_T, are presented in references 10 and 11, respectively. These parameters, which indicate the tendency of a flow with adverse pressure gradients to separate, are associated with incompressible two-dimensional laminar and turbulent boundary layers. They are functions of the velocity gradient along the flow surface, the boundary-layer momentum thickness, and the Reynolds number based on momentum thickness. In order to use these parameters in the analysis of flow separation from the suction surface of the subject blading, it was assumed that the velocities and the velocity distributions on both blades at a given incidence angle were correspondingly the same. All analytical work with these parameters gave results that were not consistent with all the data presented in this report. This may have been due to several factors. These parameters are for two-dimensional incompressible flow only and evidently cannot be used to describe three-dimensional compressible-flow phenomena. Also, it was tacitly assumed that the blade

row that experiences flow separation or stall first will probably also encounter rotating stall or surge first. Sufficient data are not available to prove or disprove this assumption. Also, reattachment of the boundary layer was not considered. Thus, it is conceivable that the long-chord blade may experience boundary-layer separation first, but also reattachment, while the short-chord blade row encounters rotating stall shortly after the boundary layer separates.

Another method of attack is to think of subsonic diffusion occurring whenever there is an increase in through-flow area per unit length in the direction of flow. If a blade passage is "equated" to a geometrically simple configuration such as a truncated cone, a dimensionless equivalent diffusion parameter D_{eq} can be obtained. Then the "rate" of diffusion can be likened to a change in an equivalent length perpendicular to the flow direction per unit length in the direction of flow. From appendix B, the equivalent diffusion parameter is

$$D_{eq} = \frac{\Delta r_{eq}}{\Delta l} = \frac{1}{\cos \overline{\gamma^{o}}} \sqrt{\frac{\overline{\mathscr{A}}}{\sigma \pi}} \left(\sqrt{\cos \overline{\beta_2'}} - \sqrt{\cos \overline{\beta_1'}} \right) \tag{B7}$$

The quantities involved in D_{eq} are defined in appendixes A and B and in figure 12.

Considering $\overline{\beta_2'}$ and $\overline{\beta_1'}$ correspondingly the same for both blade designs under consideration gives

$$D_{eq} = \frac{\Delta r_{eq}}{\Delta l} = K \sqrt{\overline{\mathscr{A}}}$$

Thus, in the three-dimensional analysis, $\Delta r_{eq}/\Delta l$ will be higher for the higher-aspect-ratio blade. In reality, the flow will separate from the suction surface only. However, this parameter considers only an "average" diffusion from the suction and pressure surfaces and from the inner and outer casing. An equivalent cone is sketched in figure 13. From the figure, the "equivalent-cone" average diffusion angle θ^{o} can be considered equal to the arc tangent of $\Delta r_{eq}/\Delta l$. It is well known that, when θ^{o} in a conical diffuser exceeds a given value (depending upon area ratio), separation will take place along the walls of the diffuser. The $\Delta r_{eq}/\Delta l$ should indicate the tendency of a given blade row to experience separation at a given operating point. However, until more data are correlated, $\Delta r_{eq}/\Delta l$ cannot be considered as supplying a quantitative "limiting" equivalent-cone angle.

[redacted]

A plot of θ^{O} against $w_{o}\sqrt{\theta_{o}}/\delta_{o}$ is given in figure 14. At each speed, θ^{O} has been computed for the three points nearest rotating stall. The angle θ^{O} for the short-chord rotor is about 4^{O} higher than that for the long-chord rotor at the point nearest stall. According to the theory, θ^{O} at stall should be the same for both blade rows. This discrepancy can be explained by the fact that the theory considers an "average" diffusion from all four surfaces of the blade passage.

Consistent correlation between the experimental data and the theories investigated could not be obtained. However, the theories do indicate that aspect ratio and chord can affect the parameters considered, and a better understanding of the complicated three-dimensional flow that is present in rotating machines is required before these effects can be examined more fully and separated from each other.

SUMMARY OF RESULTS

The performance of two aerodynamically similar single-stage rotors of different chord length has been compared. The short-chord rotor was of a design typical for a last stage of a multistage compressor. The following results were obtained:

1. At any equivalent weight flow the long-chord rotor has a higher mass-averaged total-pressure ratio than the short-chord rotor.

2. Mass-averaged peak temperature-rise efficiencies were essentially the same for both rotor designs.

3. The stall- and surge-free equivalent-weight-flow range of the long-chord rotor is greater than that of the short-chord rotor for all speeds.

4. The stall and surge characteristics of both rotors are essentially the same. Abrupt stall is experienced with a corresponding lowering of pressure ratio to the same value for both rotors.

5. A small Reynolds number effect accounted for only a part of the difference in performance in the range of Reynolds numbers examined.

6. An analysis of various diffusion parameters indicated that the better performance of the long-chord rotor could be due to either a chord or an aspect-ratio effect. More data are needed before the effects of chord and aspect ratio can be separated from each other.

Lewis Flight Propulsion Laboratory
National Advisory Committee for Aeronautics
Cleveland, Ohio, November 1, 1957

[redacted]

APPENDIX A

SYMBOLS

4536

A	area
$\mathscr{A}$	aspect ratio, ratio of blade span to chord length
b	blade span
c	chord length
D	diffusion factor
D_{eq}	equivalent diffusion parameter
D_L	separation parameter for laminar boundary layer
D_T	separation parameter for turbulent boundary layer
H	total enthalpy
i	incidence angle, angle between inlet-air direction and tangent to blade mean camber line at leading edge, deg
K	constant
l	projected length of blade along axis of rotation
M	Mach number
P	total pressure
r	radius
r_{eq}	equivalent radius
s	blade spacing
U	rotor blade speed, ft/sec
V	air velocity, ft/sec
w	weight-flow rate, lb/sec
z	axial coordinate
β	air angle, angle between air velocity and axial direction, deg

[redacted]

$\Delta\beta$ air-turning angle, $\beta_1 - \beta_2$, deg

γ° blade-chord angle, angle between blade chord and axial direction, deg

δ ratio of total pressure to NACA standard sea-level pressure of 29.92 in. Hg abs

δ° deviation angle, angle between outlet-air direction and tangent to blade mean camber line at trailing edge, deg

η adiabatic temperature-rise efficiency

θ ratio of total temperature to NACA standard sea-level temperature of 518.7° R

θ° equivalent cone angle, deg

σ blade solidity, ratio of chord to spacing

$\bar{\omega}$ total-pressure-loss coefficient

Subscripts:

C compressor

eq equivalent

h hub

m mean

o stagnation conditions (orifice)

t tip

z axial direction

1 inlet station

2 outlet station

Superscripts:

' relative to rotor

— mass or radial average

APPENDIX B

EQUIVALENT DIFFUSION PARAMETER

The equivalent diffusion parameter is given by

$$D_{eq} = \frac{\Delta r_{eq}}{\Delta l} \tag{B1}$$

A typical blade passage is shown in figure I2. If $\overline{s}$ is the radial average spacing between the limiting streamlines defining a blade passage, $\overline{s}$ is the radial average blade spacing, and the other quantities are as defined in figure 12 and appendix A, an expression for the through-flow area of blade passage at entrance and exit is as follows:

$$A_C = \overline{S}b = (\overline{s} \cos \overline{\beta'})b \tag{B2}$$

The area of an equivalent three-dimensional conical diffuser is

$$A_{eq,3\text{-}D} = \pi r_{eq}^2 \tag{B3}$$

Equating (B2) and (B3) and solving for r_{eq} yield

$$r_{eq} = \sqrt{\frac{(\overline{s} \cos \overline{\beta'})b}{\pi}} \tag{B4}$$

Expanding (B1) by finite differences and using (B4) give

$$D_{eq} = \frac{\Delta r_{eq}}{\Delta l} = \frac{\sqrt{\frac{\overline{s_2} \cos \overline{\beta_2'}\, b_2}{\pi}} - \sqrt{\frac{\overline{s_1} \cos \overline{\beta_1'}\, b_1}{\pi}}}{\overline{c} \cos \overline{\gamma^o}}$$

or

$$\frac{\Delta r_{eq}}{\Delta l} = \sqrt{\frac{\overline{s_2}}{\overline{c}} \frac{b_2}{\overline{c}} \frac{\cos \overline{\beta_2'}}{\pi(\cos \overline{\gamma^o})^2}} - \sqrt{\frac{\overline{s_1}}{\overline{c}} \frac{b_1}{\overline{c}} \frac{\cos \overline{\beta_1'}}{\pi(\cos \overline{\gamma^o})^2}} \tag{B5}$$

Now, since $\overline{\sigma} = \overline{c}/\overline{s}$ and $\overline{\mathscr{A}} = b/\overline{c}$,

$$\frac{\Delta r_{eq}}{\Delta l} = \frac{1}{\sqrt{\pi(\cos^2 \overline{\gamma^o})}} \left(\sqrt{\frac{\overline{\mathscr{A}_2}}{\overline{\sigma_2}} \cos \overline{\beta_2'}} - \sqrt{\frac{\overline{\mathscr{A}_1}}{\overline{\sigma_1}} \cos \overline{\beta_1'}} \right) \tag{B6}$$

Since $\overline{\mathscr{A}_1} = \overline{\mathscr{A}_2}$ and $\overline{\sigma_1} = \overline{\sigma_2}$ for the configurations under study,

$$D_{eq} = \frac{\Delta r_{eq}}{\Delta l} = \sqrt{\frac{\overline{\mathscr{A}}}{\overline{\sigma}\pi(\cos \overline{\gamma^o})^2}} \left(\sqrt{\cos \overline{\beta_2'}} - \sqrt{\cos \overline{\beta_1'}} \right) \tag{B7}$$

4536

REFERENCES

1. Members of the Compressor and Turbine Research Division: Aerodynamic Design of Axial-Flow Compressors. Vol. II. NACA RM E56B03a, 1956.

2. Graham, Robert W., and Prian, Vasily D.: Experimental and Theoretical Investigation of Rotating-Stall Characteristics of Single-Stage Axial-Flow Compressor with Hub-Tip Ratio of 0.76. NACA RM E53I09, 1953.

3. Ossofsky, Eli: Constant Temperature Operation of the Hot-Wire Anemometer at High Frequency. Rev. Sci. Instr., vol. 19, no. 12, Dec. 1948, pp. 881-889.

4. Laurence, James C., and Landes, L. Gene: Auxiliary Equipment and Techniques for Adapting the Constant-Temperature Hot-Wire Anemometer to Specific Problems in Air-Flow Measurements. NACA TN 2843, 1952.

5. Huppert, Merle C.: Preliminary Investigation of Flow Fluctuations During Surge and Blade Row Stall in Axial-Flow Compressors. NACA RM E52E28, 1952.

6. Huppert, Merle C., and Benser, William A.: Some Stall and Surge Phenomena in Axial-Flow Compressors. Jour. Aero. Sci., vol. 20, no. 12, Dec. 1953, pp. 835-845.

7. Sievers, Gilbert K., Geye, Richard P., and Lucas, James G.: Preliminary Analysis of Over-All Performance of an Eight-Stage Axial-Flow Research Compressor with Two Long-Chord Transonic Inlet Stages. NACA RM E57H14, 1957.

[redacted]

8. Eckert, B.: Axialkompressoren und Radialkompressoren. Ch. V, secs. 3, 4, and 5, Springer-Verlag (Berlin), 1953.

9. Neustein, Joseph: Experiments at Low Reynolds Numbers. Pt. II. Axial Flow Turbomachine. Rep. No. 6, Hydrodynamics and Mech Eng. Labs., C.I.T., Mar. 1957. (Navy Contract Nonr-220(23), NR 097-001.)

10. Loitsianski, L. G.: Approximate Method of Integration of Laminar Boundary Layer in Incompressible Fluid. NACA TM 1293, 1951.

11. Kalikhman, L. E.: A New Method for Calculating the Turbulent Boundary Layer and Determining the Separation Point. Comptes Rendus (Doklady), de I'Acad. des Sci. de l'URSS, vol. XXXVIII, no. 5-6, 1943, pp. 165-169.

TABLE I. - ROTOR DESIGN GEOMETRY

	Short-chord	Long-chord		Both rotors
Chord length, c, in.	0.67	1.67	Relative inlet-air angle, β_1', deg	
			r = 5.6"	60.7
Aspect ratio, $\mathscr{A}$	2.09	0.84	r = 6.3"	62.6
			r = 7.0"	65.0
Number of blades	66	26		
			Incidence angle, i, deg	
Tip solidity, σ_t	1.005	0.987	r = 5.6"	7.6
			r = 6.3"	5.9
Hub radius, r_h, in.	5.60	5.60	r = 7.0"	3.4
Tip radius, r_t, in.	7.00	7.00	Deviation angle, δ^o, deg	
			r = 5.6"	5.3
Hub-tip radius ratio, r_h/r_t	0.8	0.8	r = 6.3"	3.8
			r = 7.0"	2.8
Passage height, in.	1.40	1.40		
			Air-turning angle, $\Delta\beta$, deg	
Hub thickness-to-chord ratio	0.12	0.12	r = 5.6"	10.8
			r = 6.3"	9.8
Tip thickness-to-chord ratio	0.10	0.10	r = 7.0"	8.5
Leading- and trailing-edge radii, in.	0.010	0.010	Approx. blade solidity, σ	
			r = 5.6"	1.3
Fillet radius, in.	0.125	0.125	r = 6.3"	1.1
			r = 7.0"	1.0
Tip speed, $U_t/\sqrt{\theta}$, ft/sec	850	850		

TABLE II. - STALL HISTORIES OF SHORT- AND LONG-CHORD ROTORS

Equivalent speed, $U_t/\sqrt{\theta}$, ft/sec	Absolute propagation rate	Surge or stall frequency, cps	Observation (as flow is decreased)[1]
Short-chord rotor			
450	0.595	75	(1) Rotating stall, 1 zone (2) Rotating stall, 2 zones (3) Rotating stall, 3 zones (4) Rotating stall, 4 zones
550	0.604	93 ↓ 4 93 60 120 60	(1) Rotating stall, 1 zone (2) Rotating stall, 2 zones (3) Rotating stall, 3 zones (4) (a) Rotating stall, 4 zones (b) Audible intermittent surge (5) (a) Rotating stall, 4 zones (b) Surge, frequency I (c) Surge, frequency II (6) Surge
650	0.578	105 ↓ 78 4 78 4 78	(1) Rotating stall, 1 zone (2) Rotating stall, 2 zones (3) Rotating stall, 3 zones (4) (a) Rotating stall, 4 zones (b) Surge (c) Audible surge (5) (a) Surge (b) Audible surge (6) Surge
750	0.594	124 ↓ 26 87.5 4 87.5	(1) Rotating stall, 1 zone (2) Rotating stall, 2 zones (3) (a) Rotating stall, 2 zones (b) Surge (4) (a) Surge (b) Audible intermittent surge (5) Surge
850	0.568	135 135 26 96 4 98	(1) Rotating stall, 1 zone (2) Rotating stall, 2 zones (3) Surge (4) (a) Surge (b) Audible intermittent surge (5) Surge
Long-chord rotor			
450	0.640	80 80 12	(1) Rotating stall, 1 zone (2) Rotating stall, 2 zones (3) Surge
550	0.636	98 98 4.5	(1) Rotating stall, 1 zone (2) Rotating stall, 2 zones (3) Audible surge
650	0.626	114 114 4.5	(1) Rotating stall, 1 zone (2) Rotating stall, 2 zones (3) Audible surge
750	0.574	120 4.5	(1) Rotating stall, 1 zone (2) Audible surge
850	-----	4.5	(1) Audible surge

[1]Listings such as (5) (a), (b), (c), indicate that, at the fifth unique operating point studied, as the flow was decreased conditions (a), (b), and (c) were observed occurring more or less simultaneously.

[redacted]

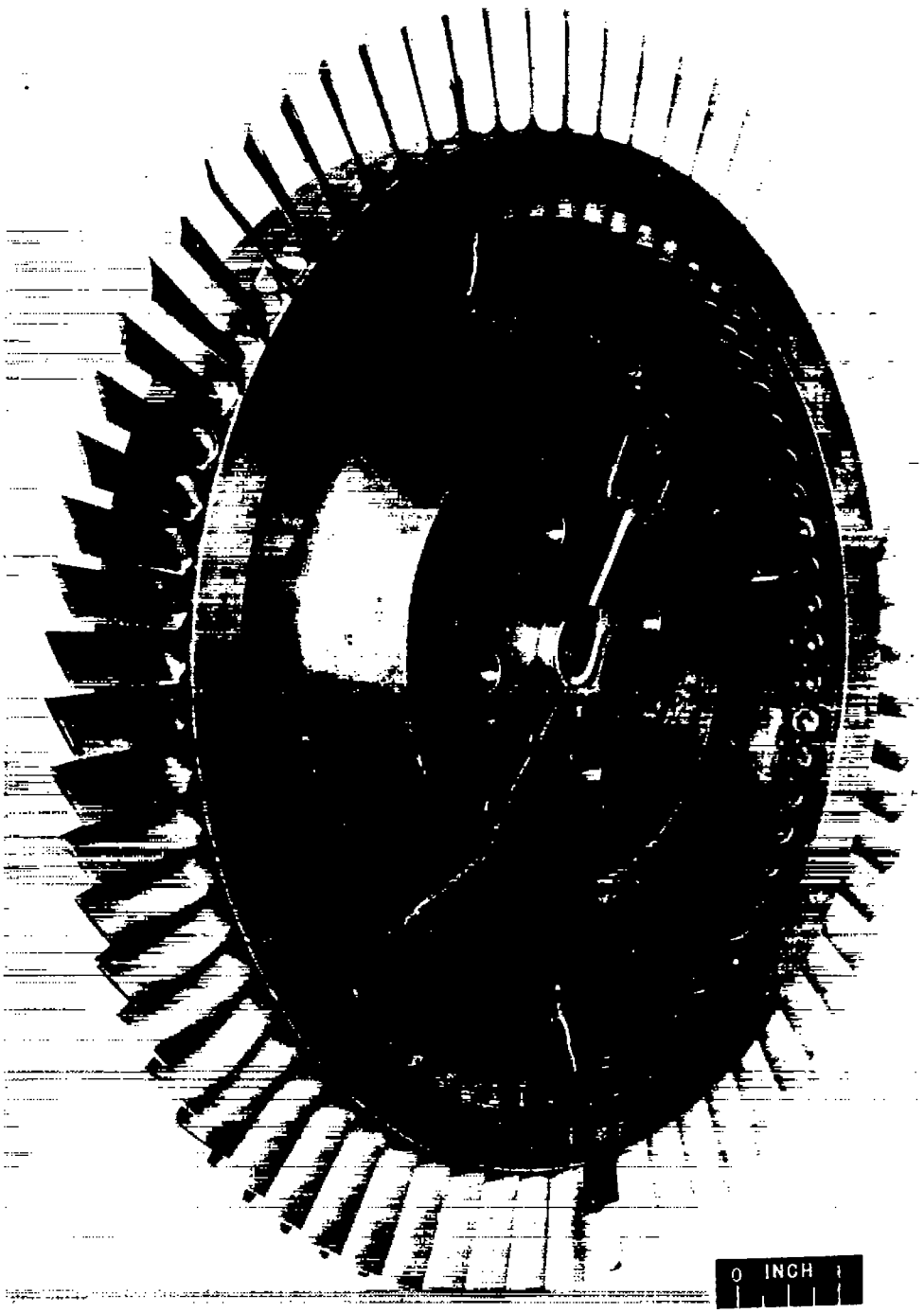

C-44979

(a) Short-chord rotor.

Figure 1. - Single-stage compressor rotors investigated.

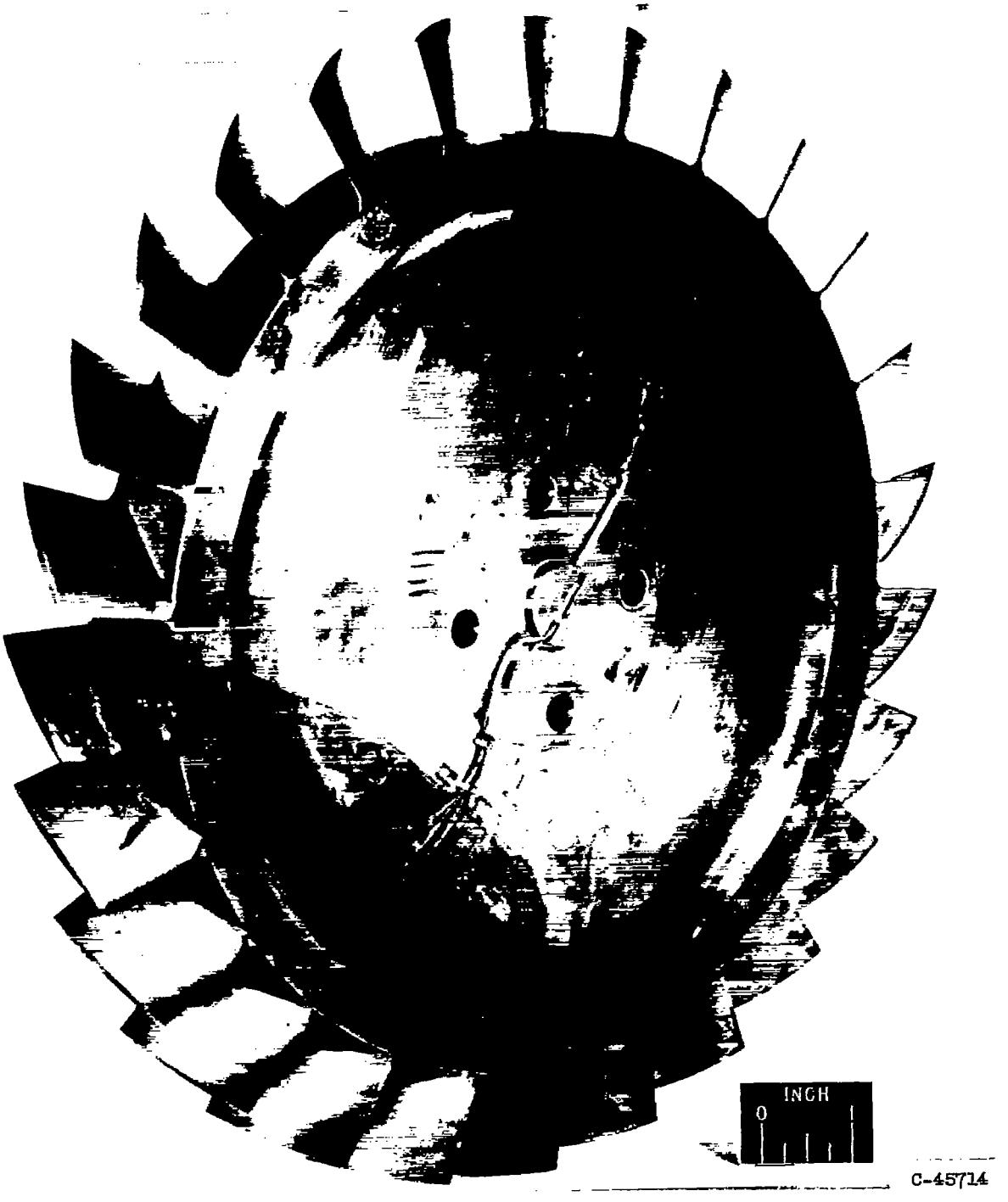

(b) Long-chord rotor.

Figure 1. - Concluded. Single-stage compressor rotors investigated.

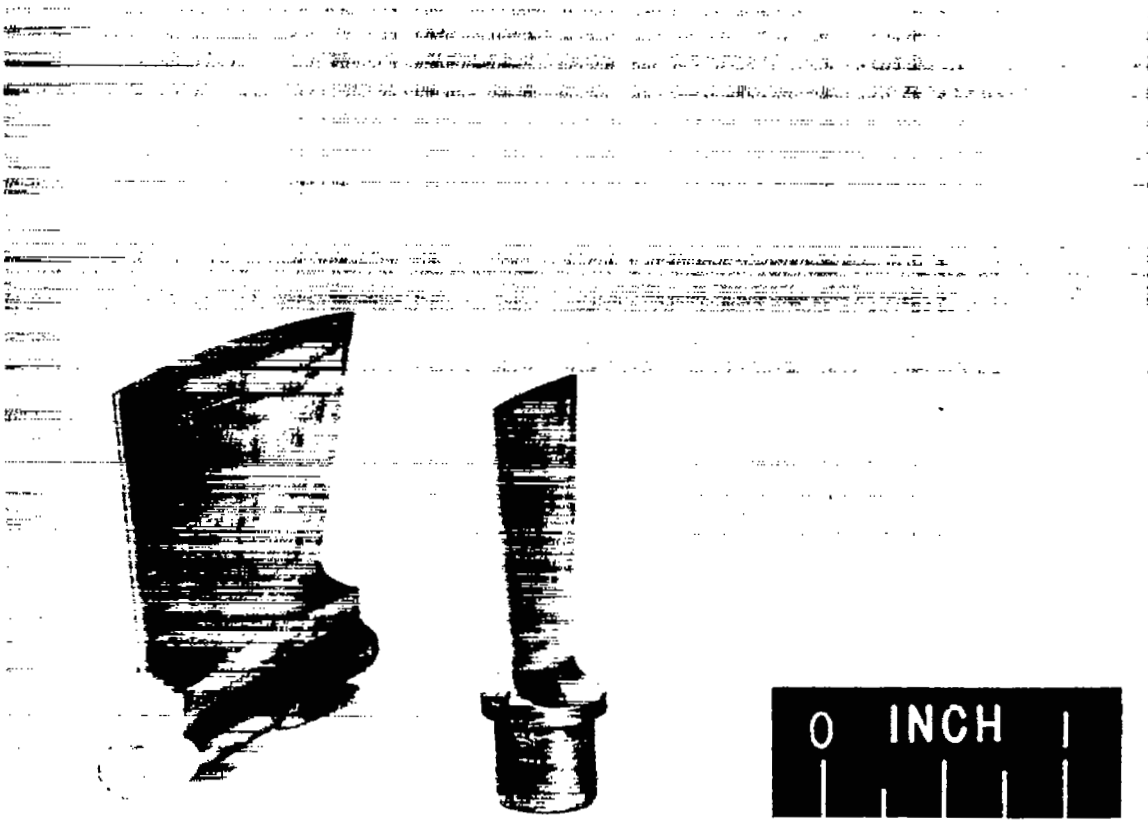

C-44980

Figure 2. - Long- and short-chord blades.

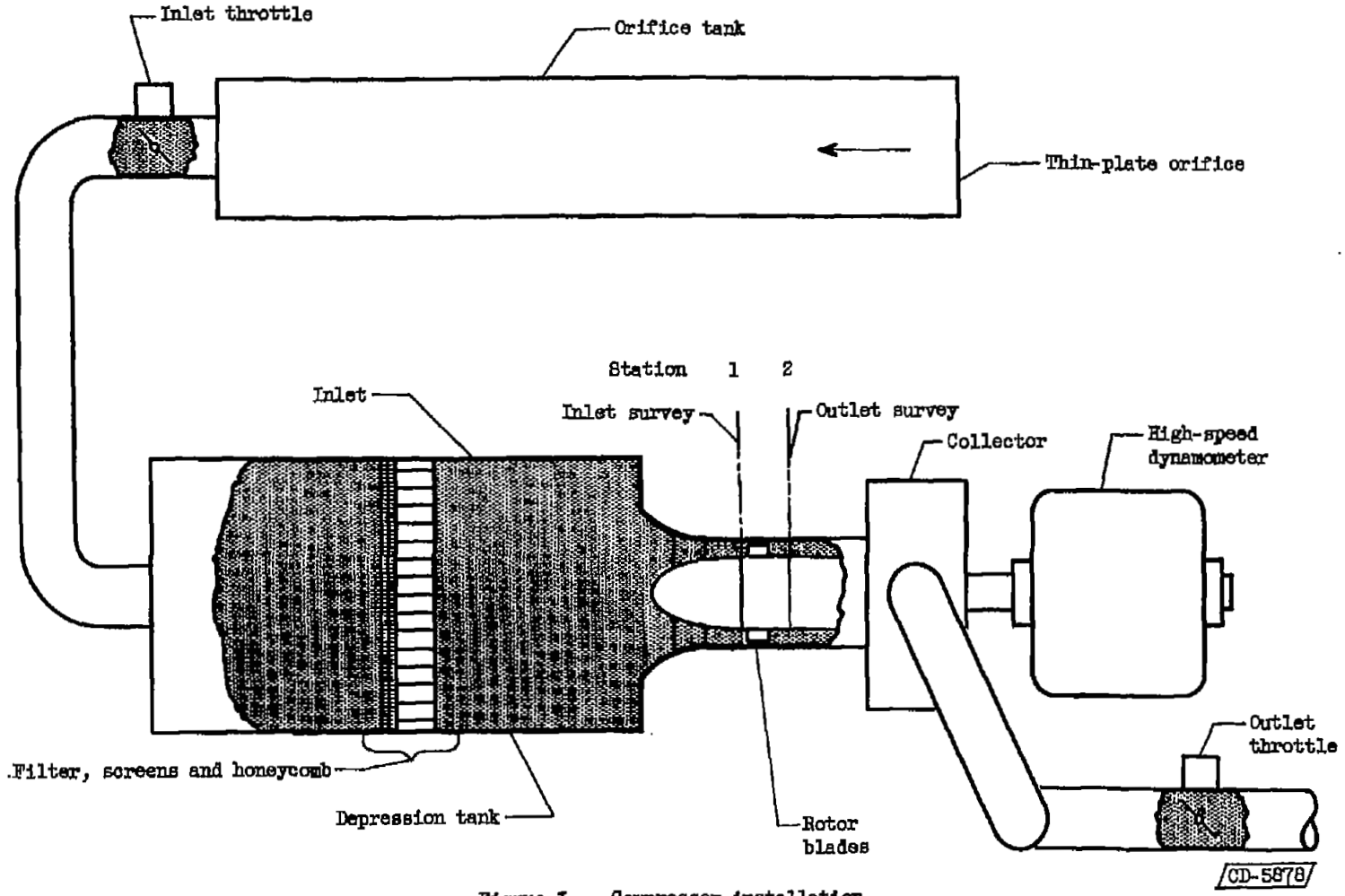

Figure 3. - Compressor installation.

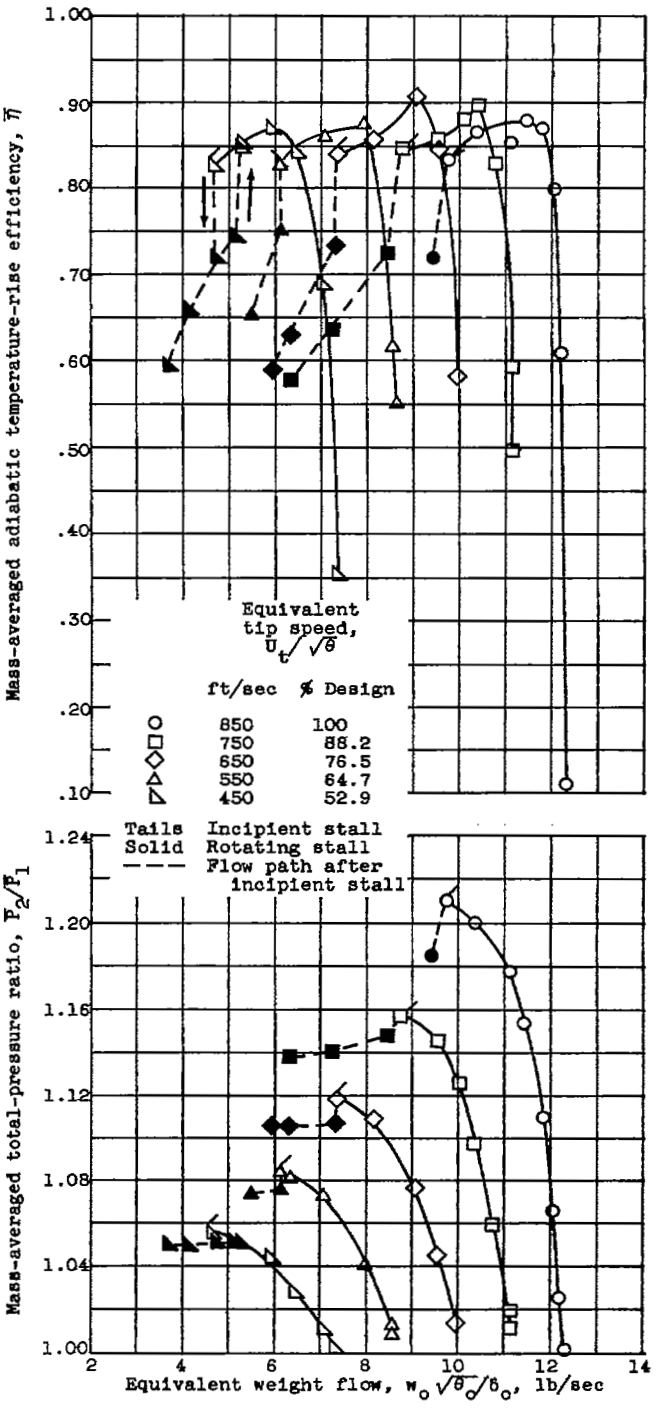

(a) Short-chord rotor.

Figure 4. - Over-all performance of rotors. Inlet pressure, 25 inches of mercury absolute.

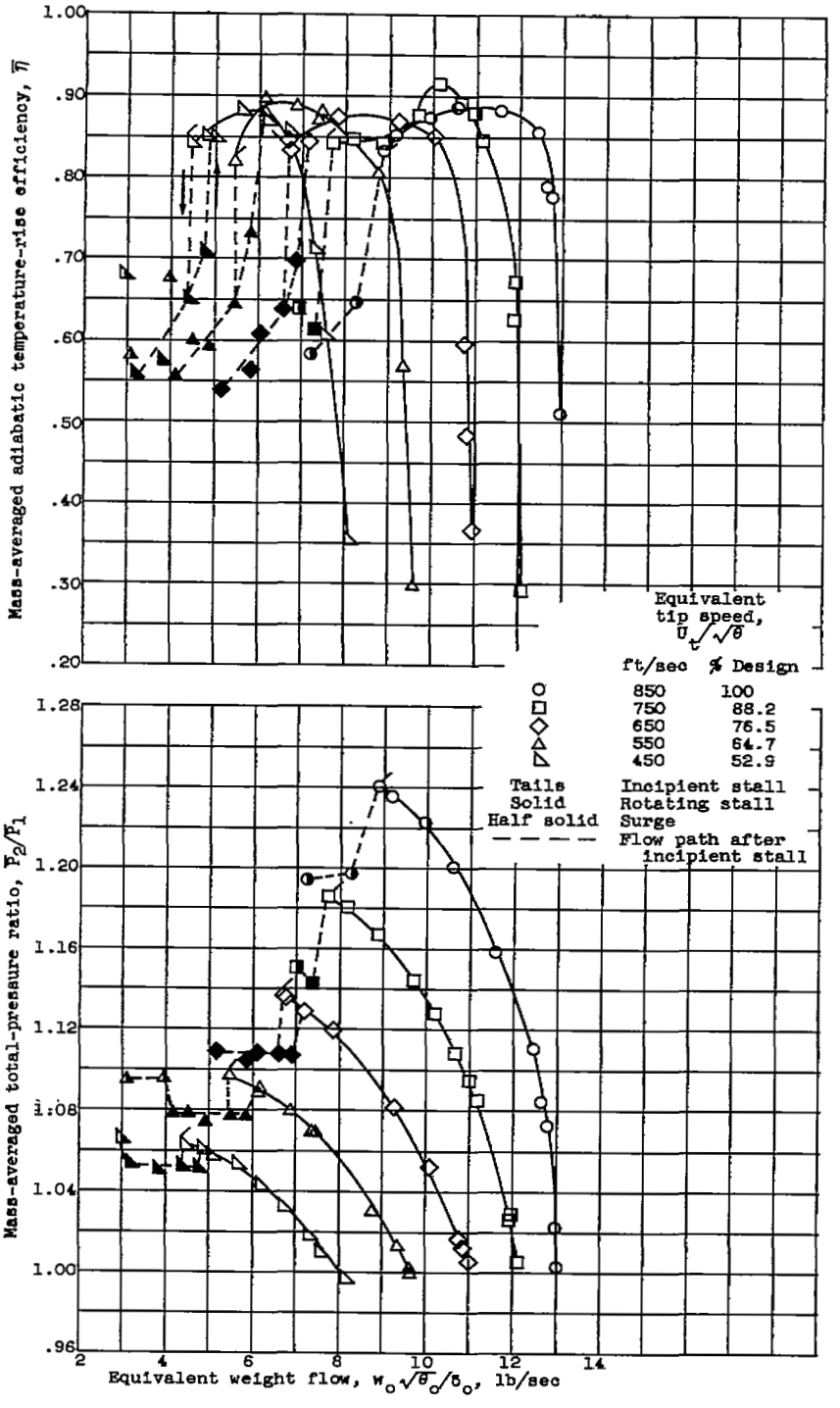

(b) Long-chord rotor.

Figure 4. - Concluded. Over-all performance of rotors. Inlet pressure, 25 inches of mercury absolute.

[redacted]

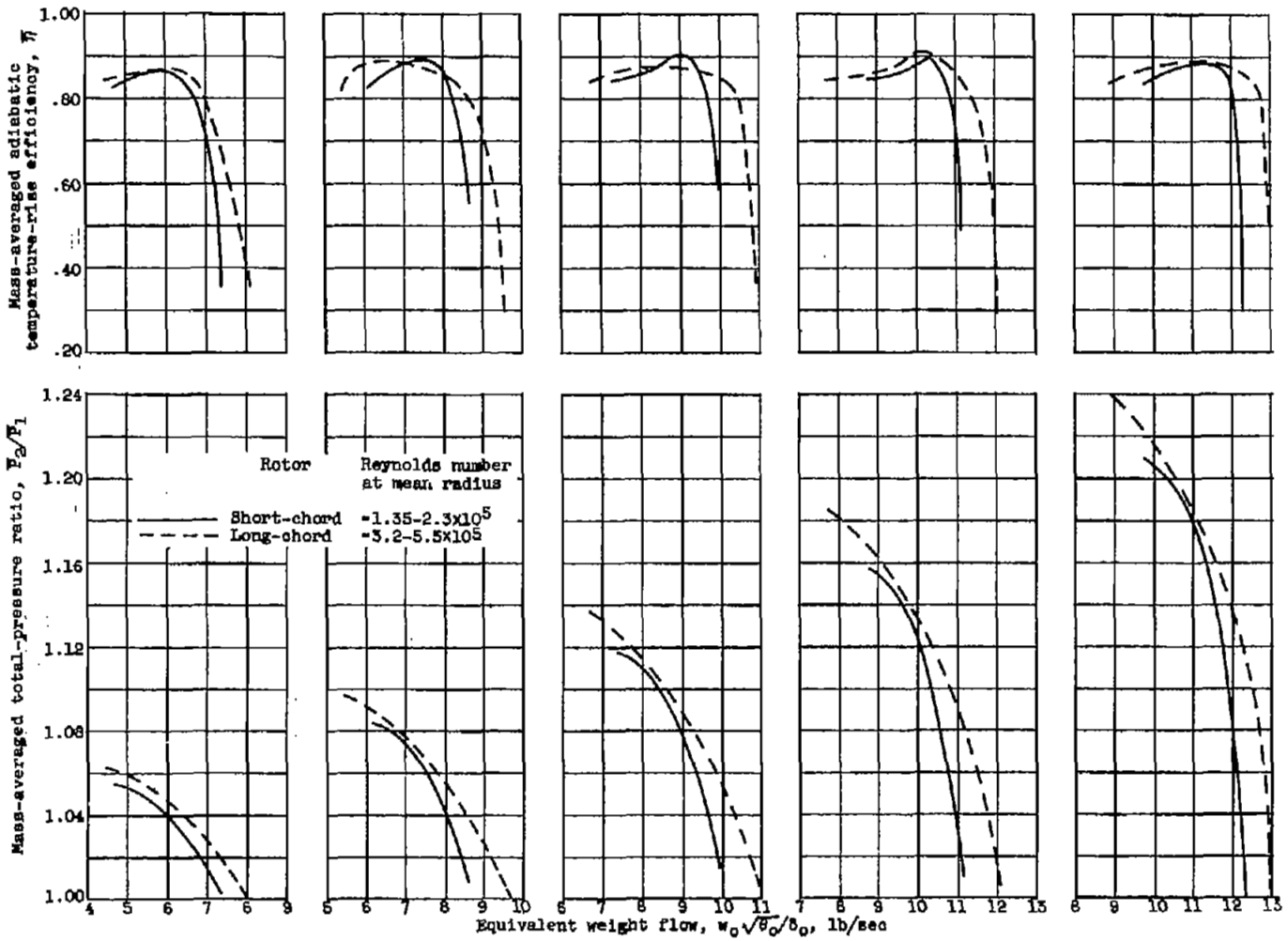

(a) $U_t/\sqrt{\theta}$ = 450 feet per second. (b) $U_t/\sqrt{\theta}$ = 550 feet per second. (c) $U_t/\sqrt{\theta}$ = 650 feet per second. (d) $U_t/\sqrt{\theta}$ = 750 feet per second. (e) $U_t/\sqrt{\theta}$ = 850 feet per second.

Figure 5. - Comparison of over-all performances of short- and long-chord rotors during unstalled operation. Inlet pressure, 23 inches of mercury absolute.

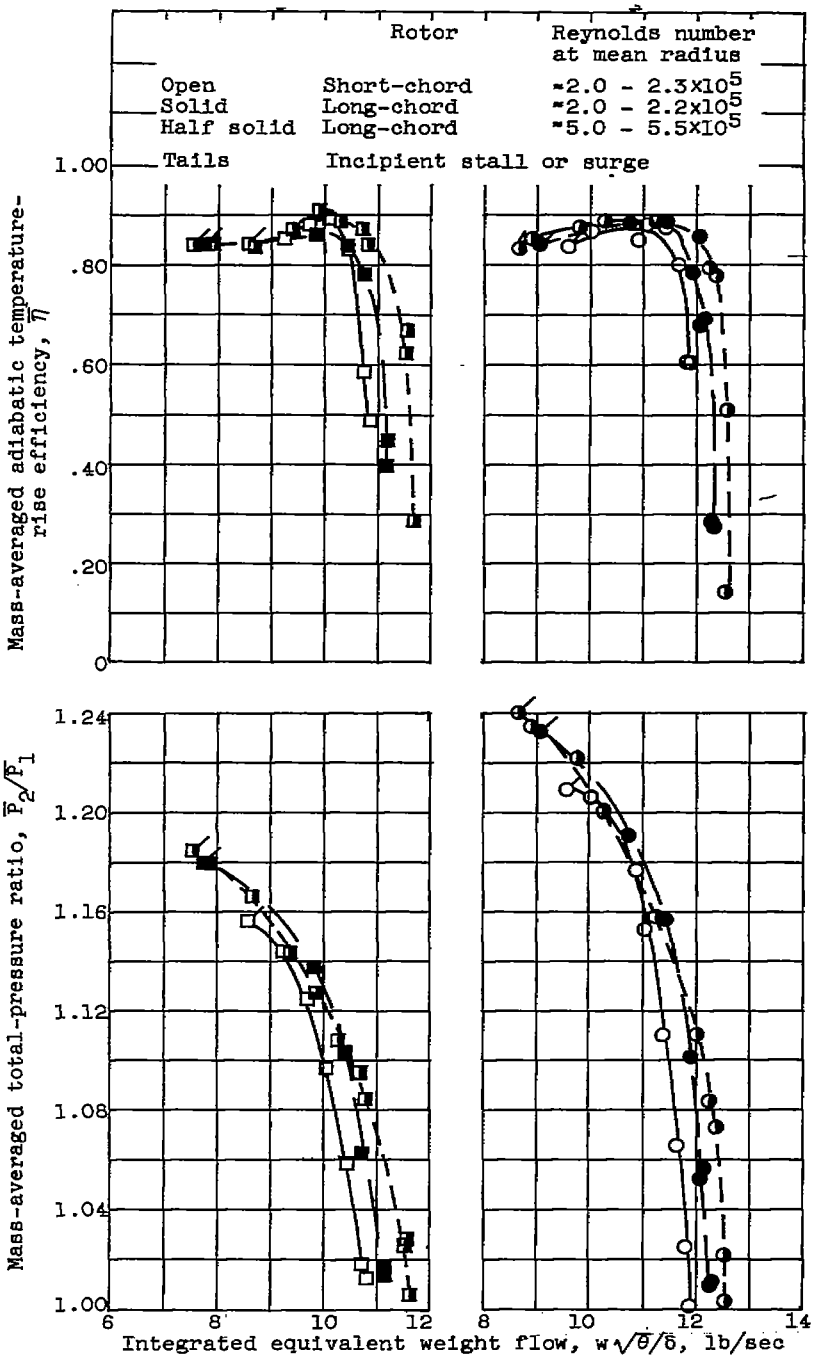

(a) $U_t/\sqrt{\theta}$, 750 feet per second.

(b) $U_t/\sqrt{\theta}$, 850 feet per second.

Figure 6. - Comparison of performance of short- and long-chord rotors during unstalled operation. Long-chord rotor at two Reynolds number ranges.

[redacted]

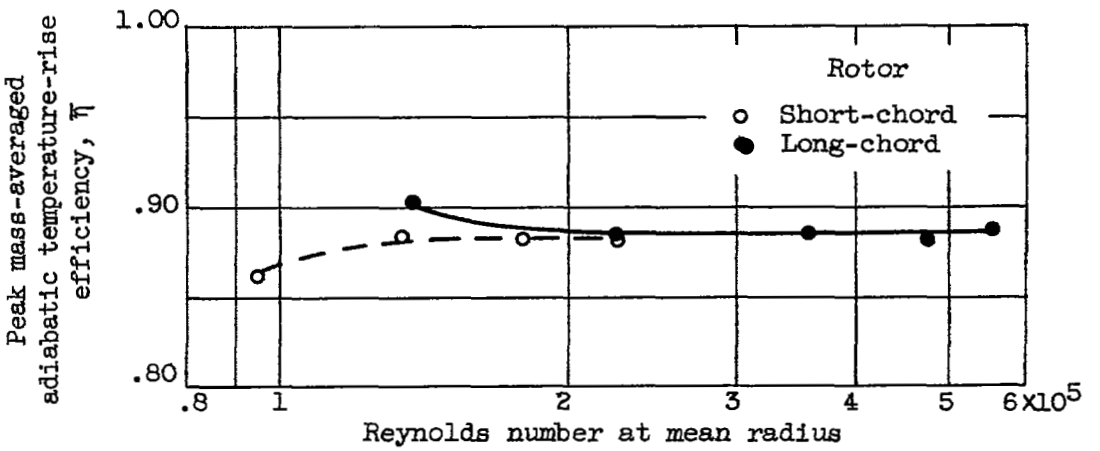

Figure 7. - Design-speed peak efficiencies of short- and long-chord rotors for various inlet pressures.

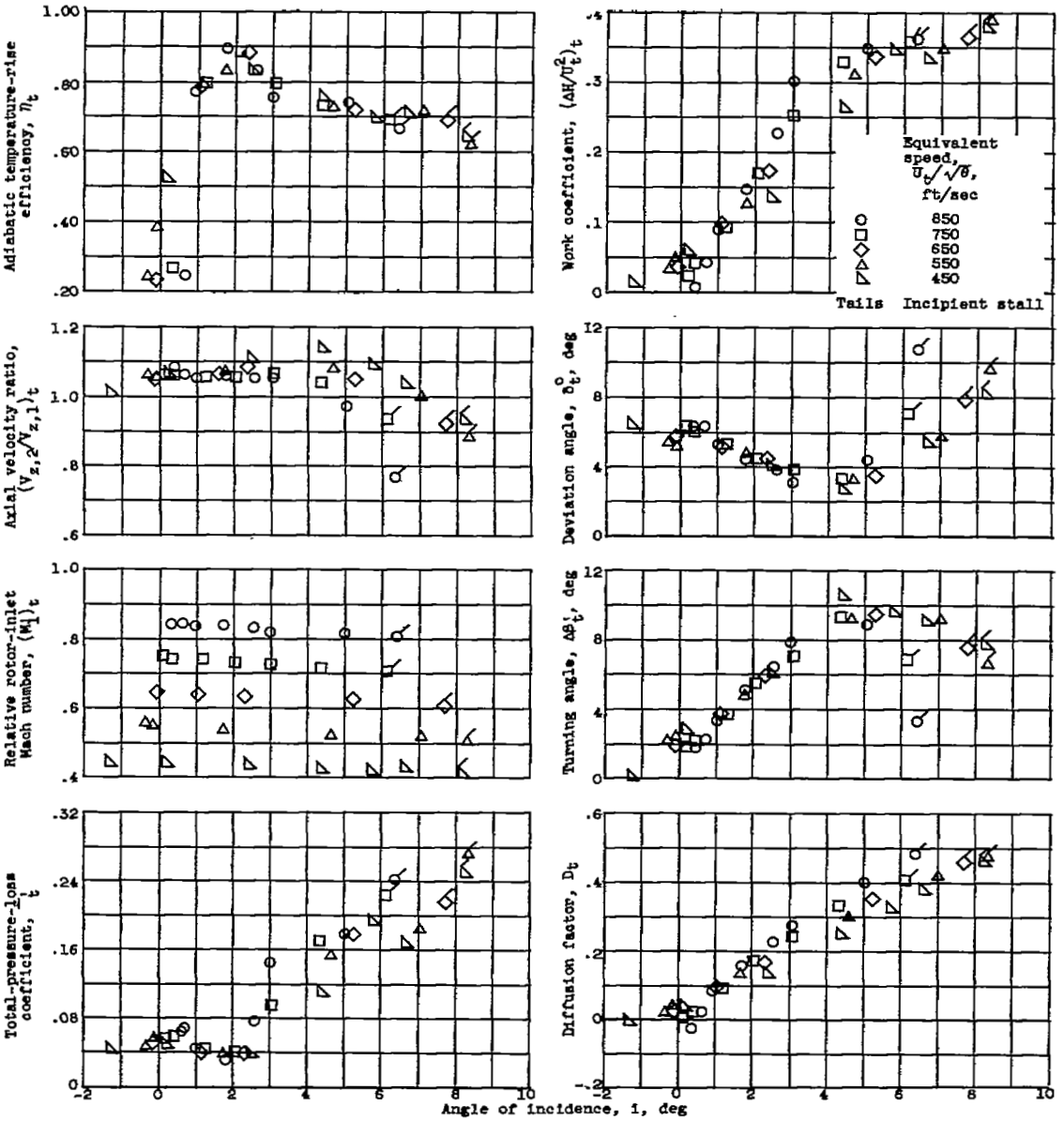

(a) Tip radius.

Figure 8. - Blade-element performance for short-chord rotor. Inlet pressure, 25 inches of mercury absolute.

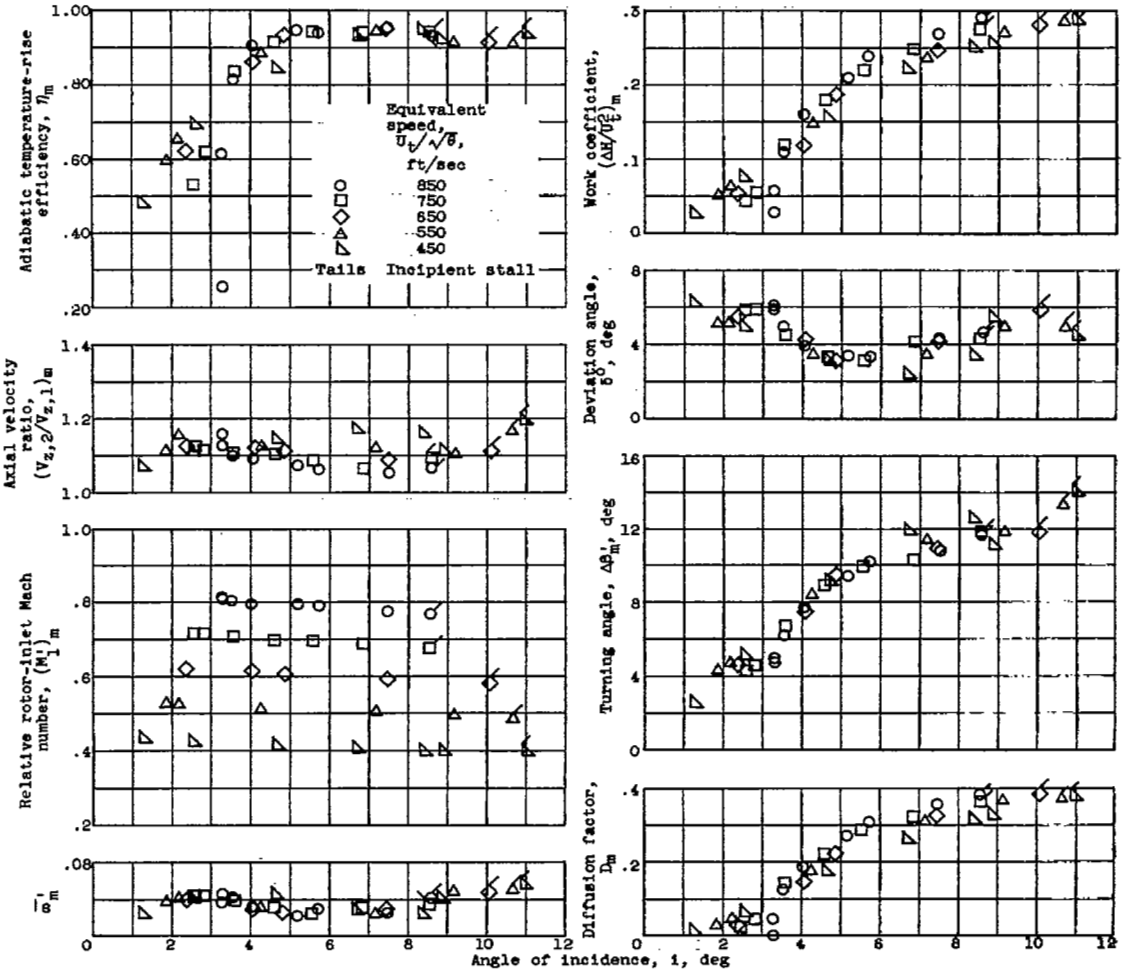

(b) Mean radius.

Figure 8. - Continued. Blade-element performance for short-chord rotor. Inlet pressure, 25 inches of mercury absolute.

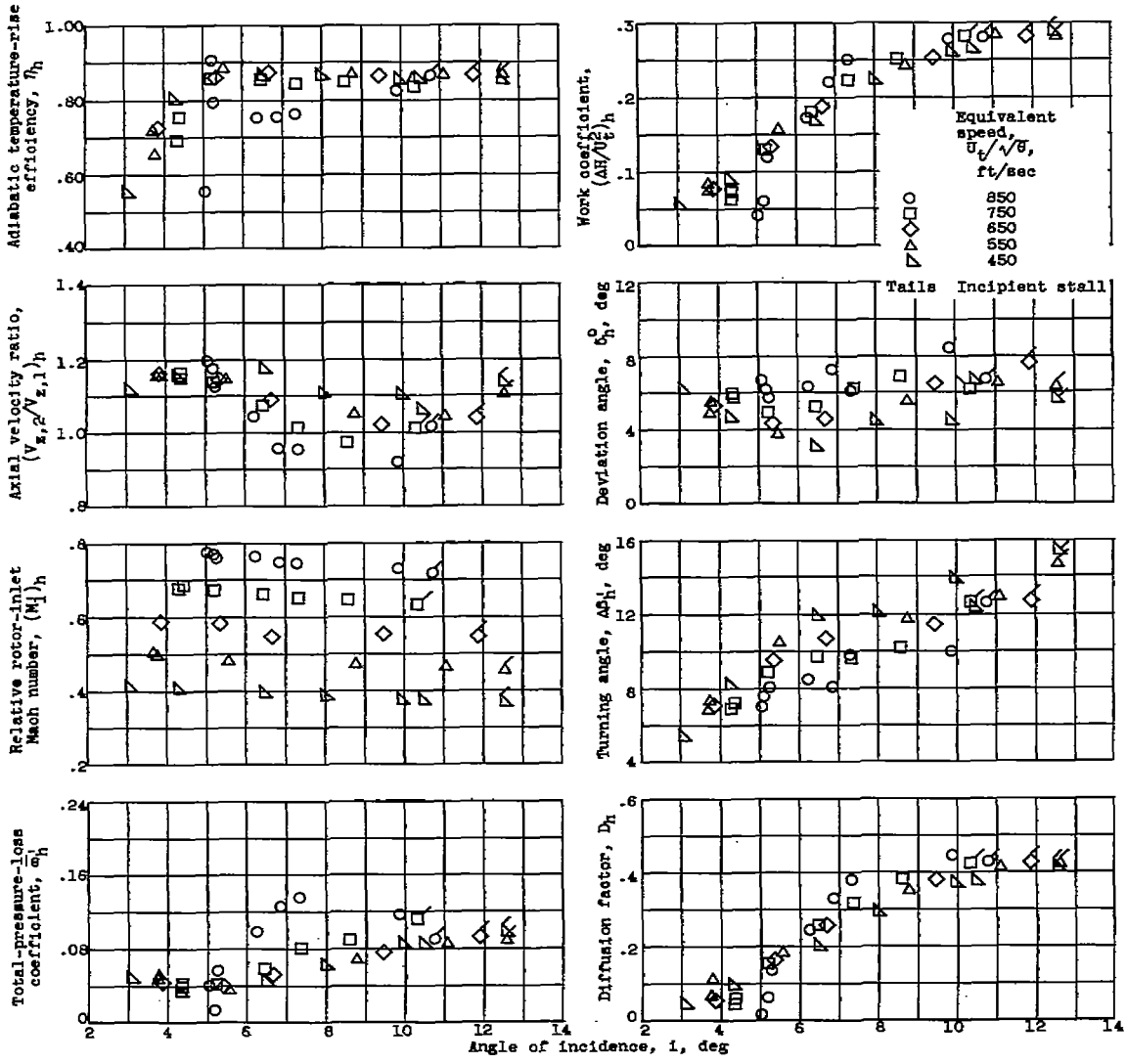

(c) Hub radius.

Figure 8. - Concluded. Blade-element performance for short-chord rotor. Inlet pressure, 25 inches of mercury absolute.

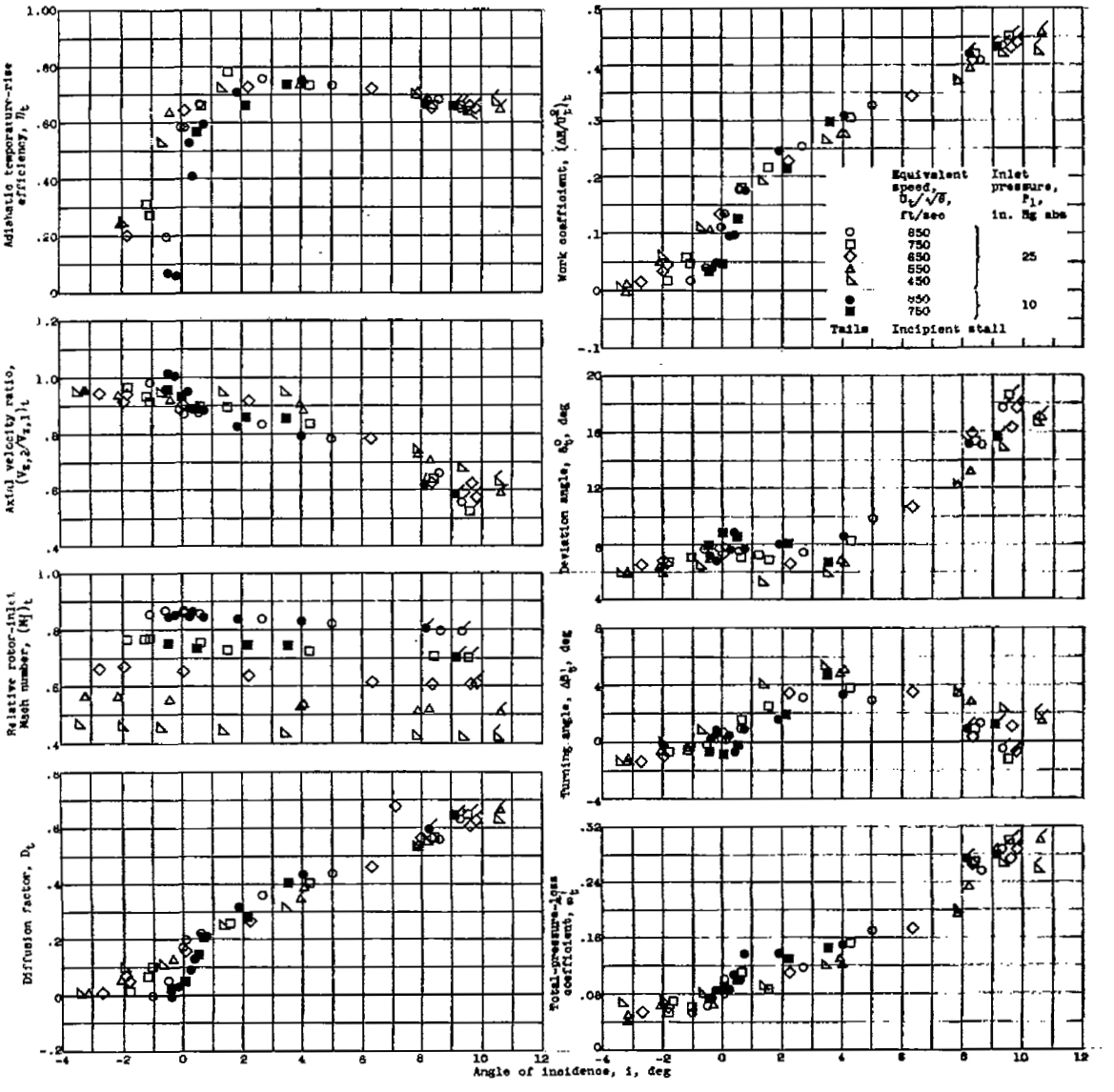

(a) Tip radius.

Figure 9. - Blade-element performance for long-chord rotor.

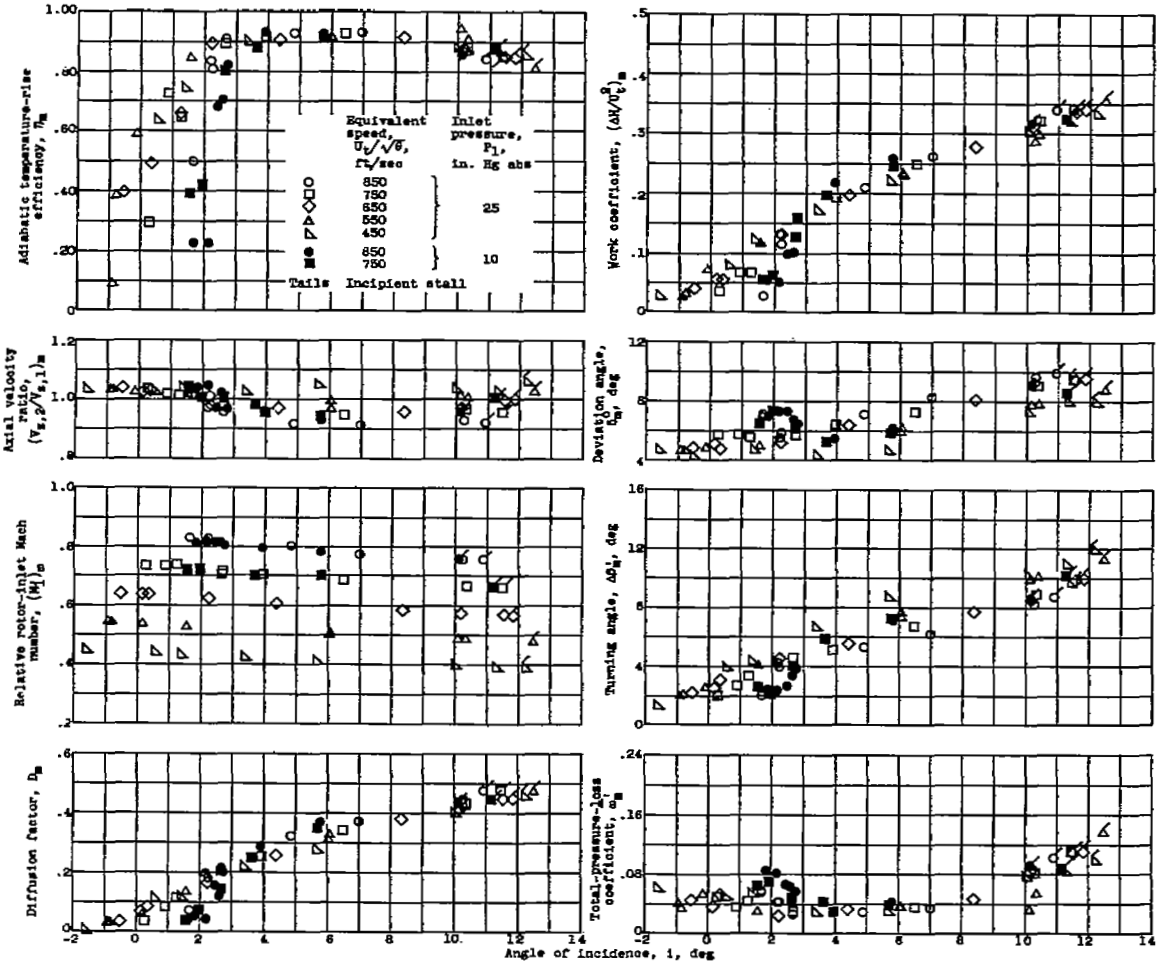

(b) Mean radius.

Figure 9. - Continued. Blade-element performance for long-chord rotor.

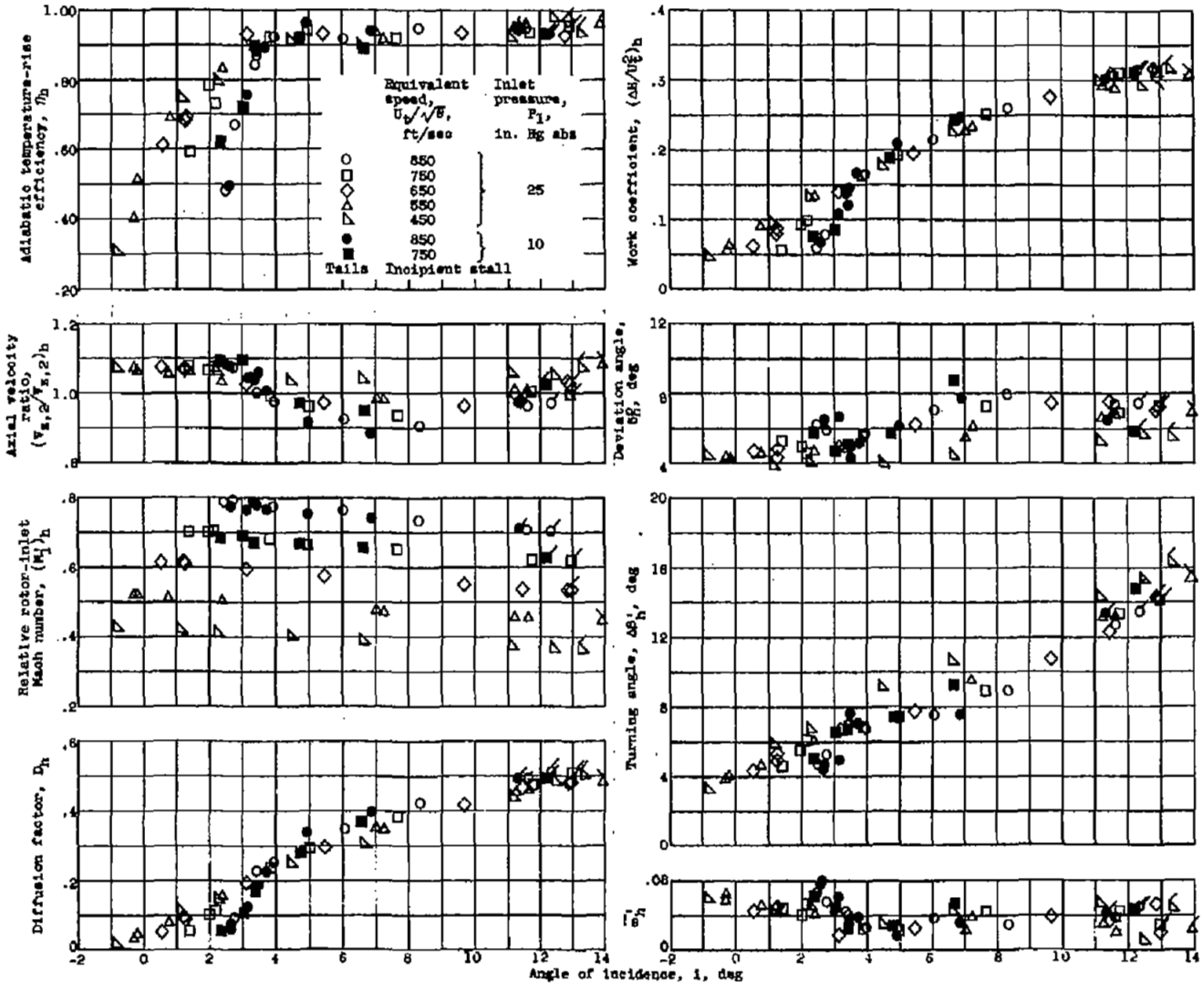

(c) Hub radius.

Figure 9. - Concluded. Blade-element performance for long-chord rotor.

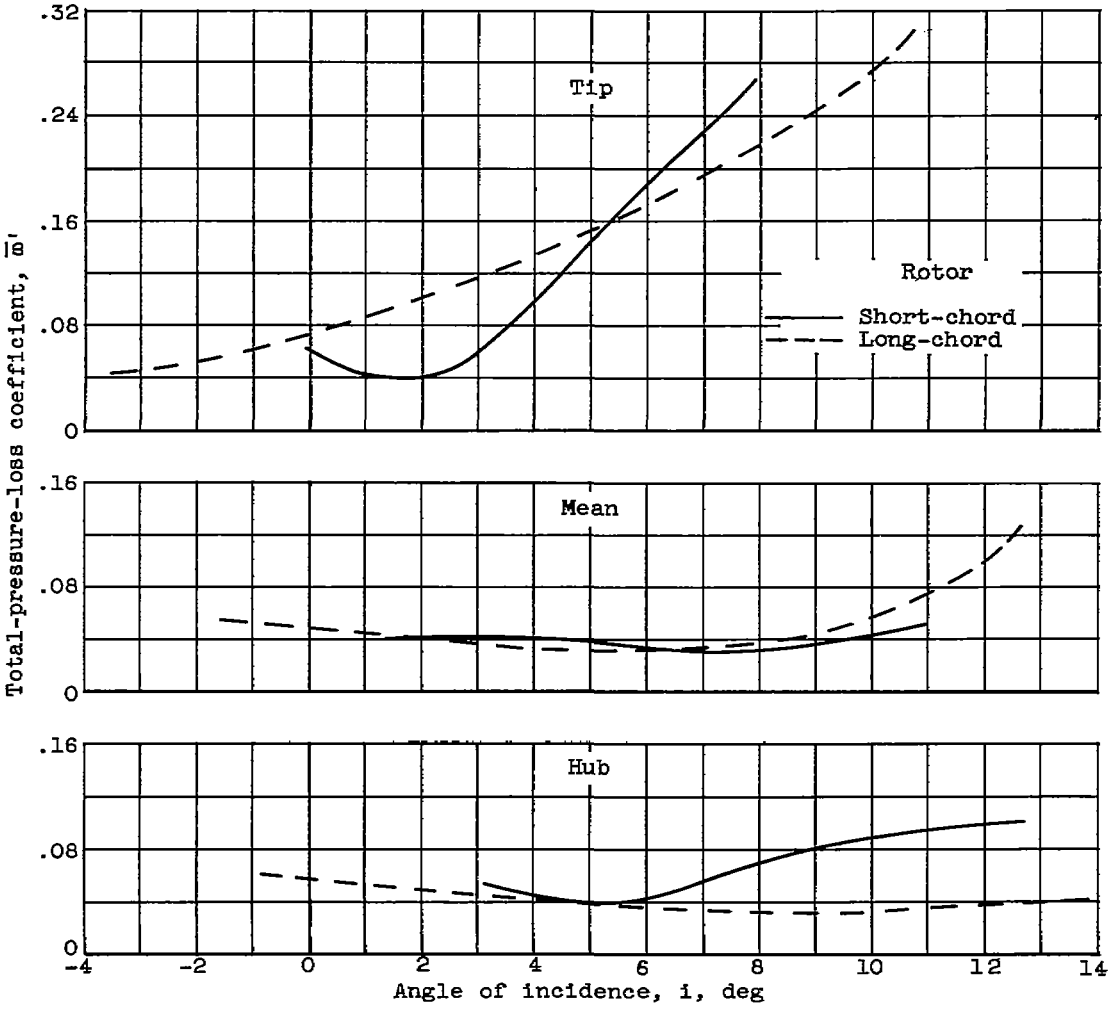

Figure 10. - Comparison of total-pressure-loss coefficients for long- and short-chord rotors.

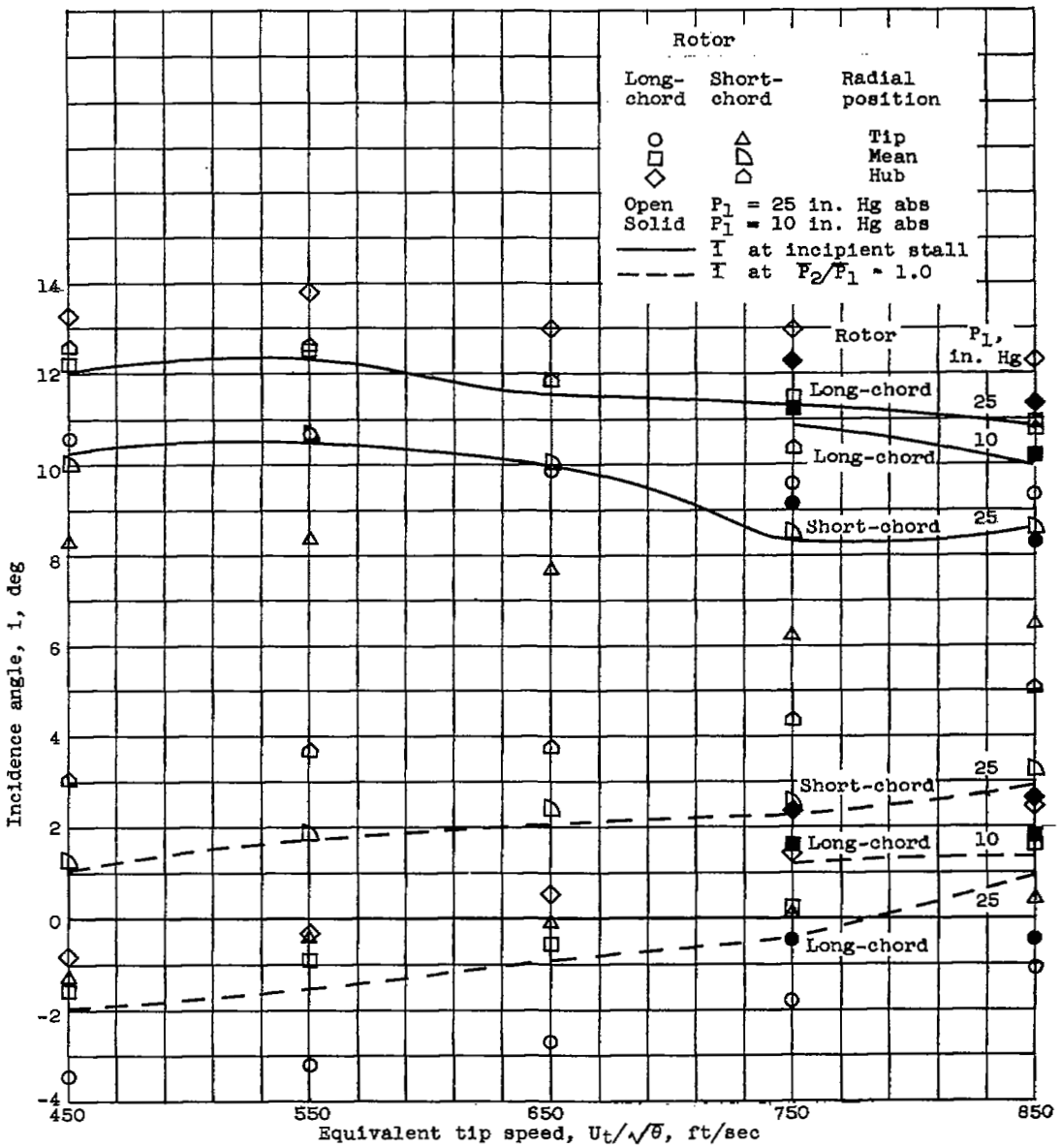

Figure 11. - Incidence angle at end points of unstalled performance data for long- and short-chord rotors at speeds tested.

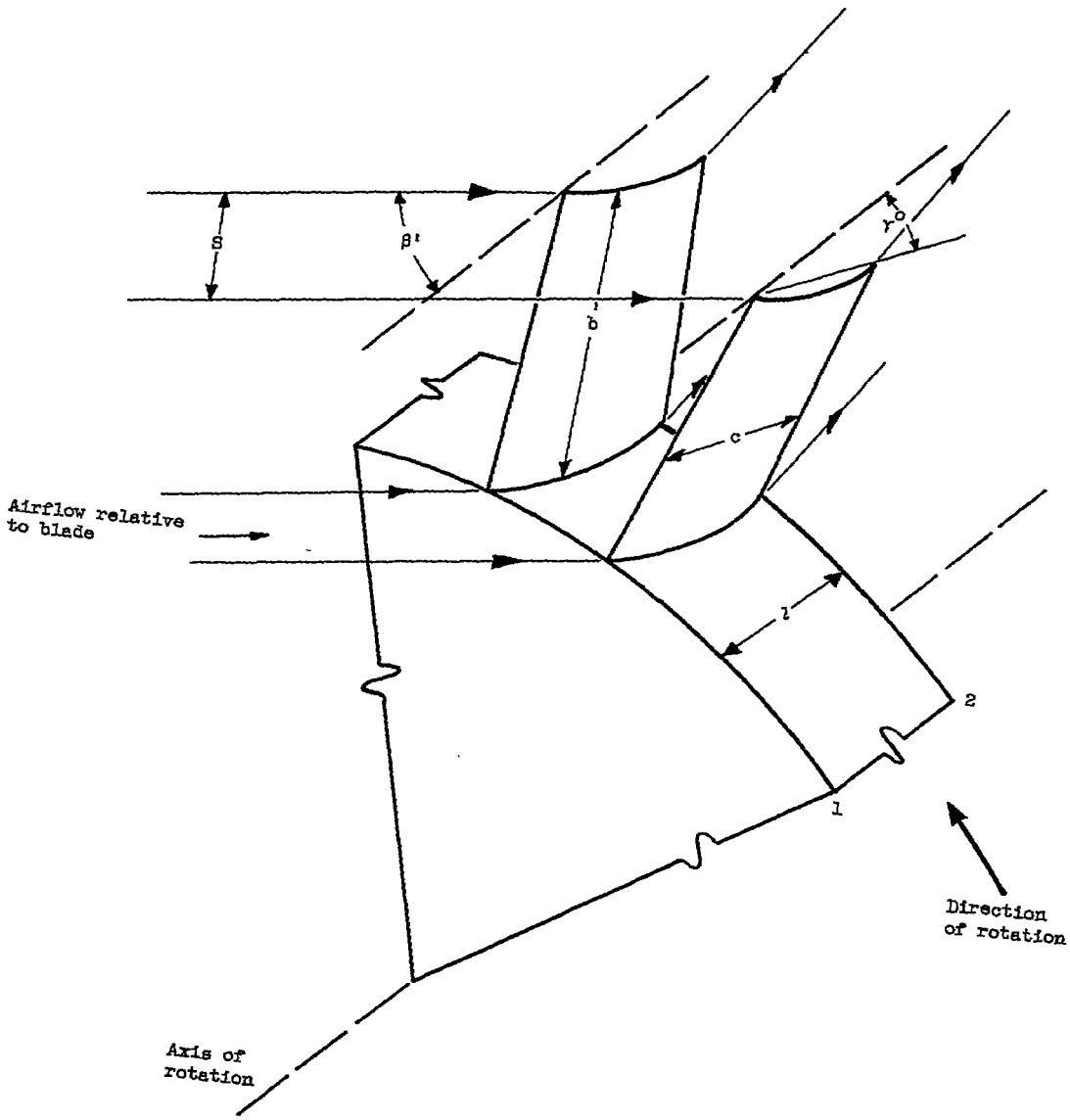

CD-5887

Figure 12. - Typical compressor blade passage.

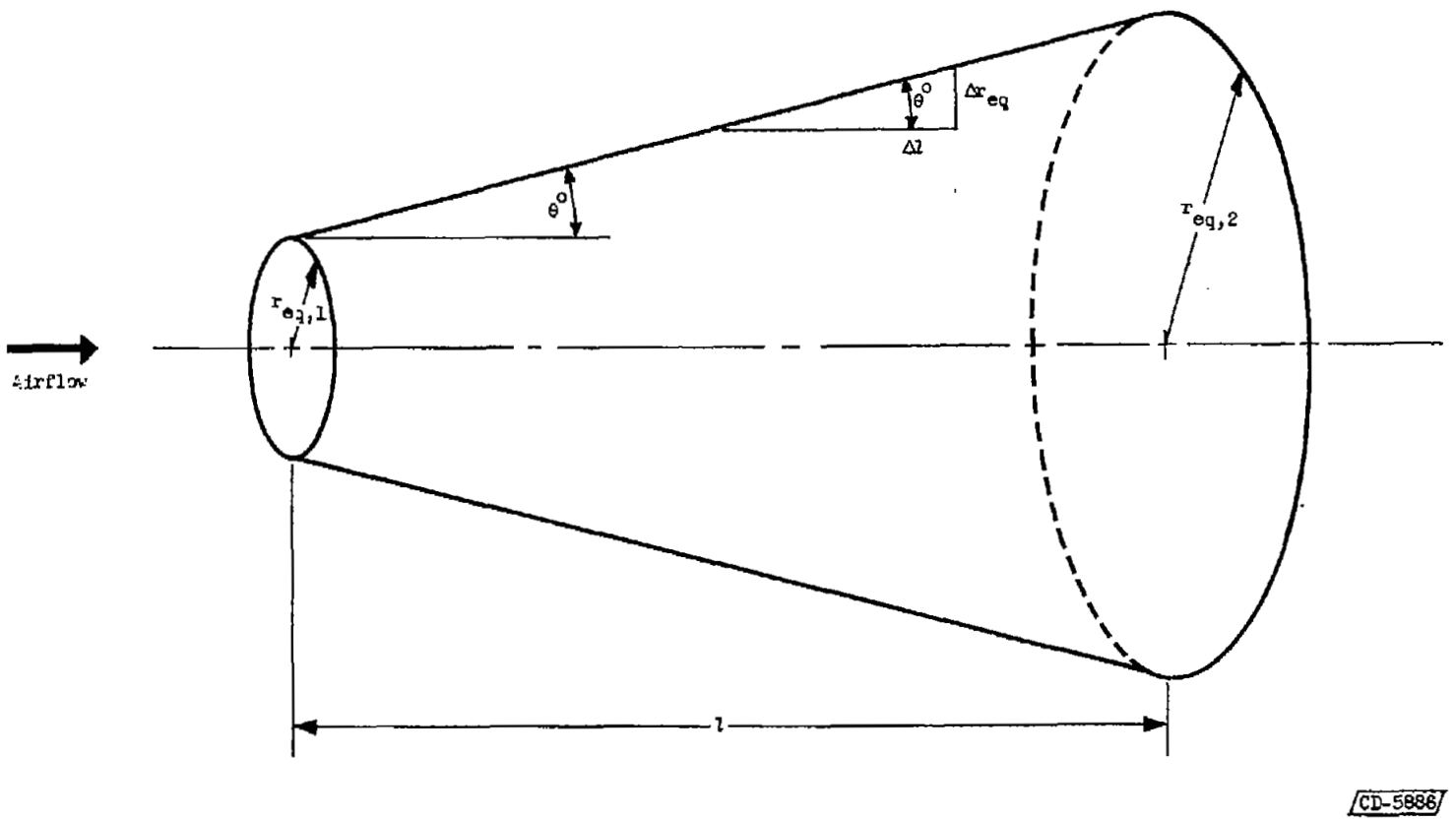

Figure 13. - Equivalent cone.

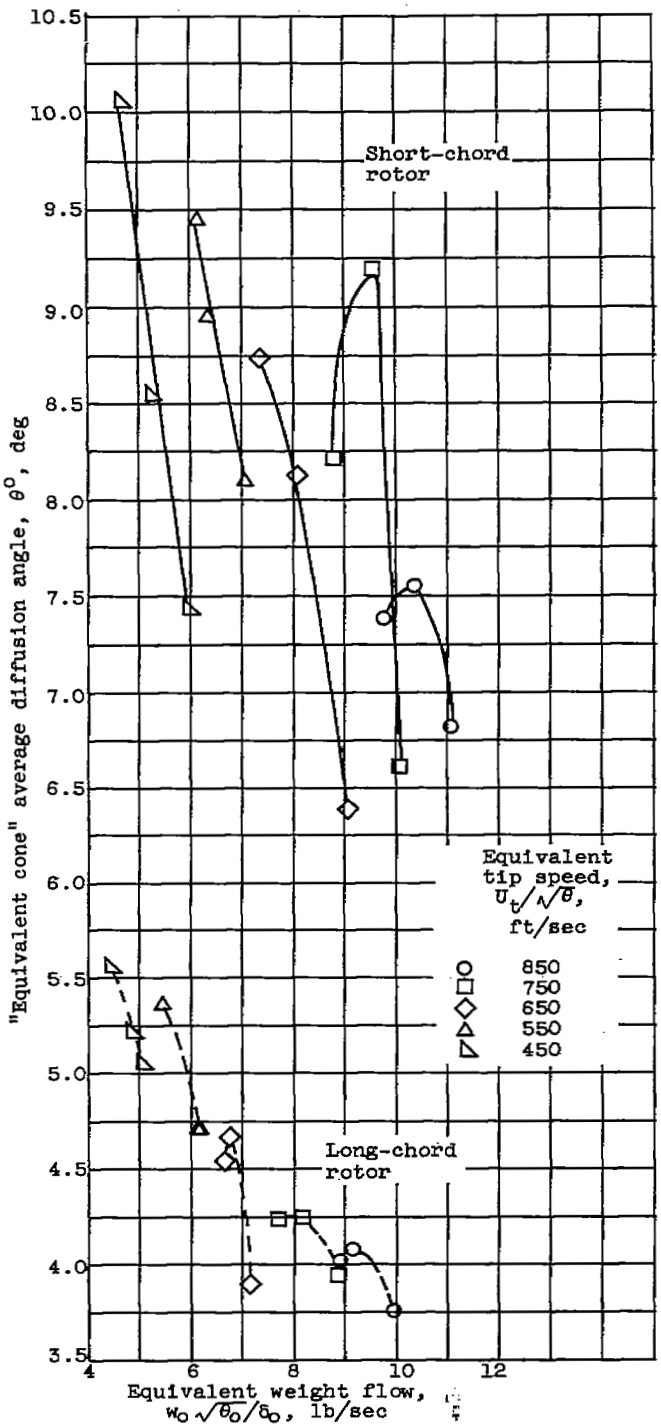

Figure 14. - Variation of equivalent cone angle with equivalent weight flow.